GLOBAL BIOGEOCHEMICAL CYCLES, VOL. 11, NO. 1, PAGES 43–76, MARCH 1997

# An inverse modeling approach to investigate the global atmospheric methane cycle

Ralf Hein[1] and Paul J. Crutzen
Abteilung Chemie der Atmosphäre, Max-Planck-Institut für Chemie, Mainz, Germany

Martin Heimann
Max-Planck-Institut für Meteorologie, Hamburg, Germany

**Abstract.** Estimates of the global magnitude of atmospheric methane sources are currently mainly based on direct flux measurements in source regions. Their extrapolation to the entire globe often involves large uncertainties. In this paper, we present an inverse modeling approach which can be used to deduce information on methane sources and sinks from the temporal and spatial variations of atmospheric methane mixing ratios. Our approach is based on a three-dimensional atmospheric transport model which, combined with a tropospheric background chemistry module, is also employed to calculate the global distribution of OH radicals which provide the main sink for atmospheric methane. The global mean concentration of OH radicals is validated with methyl chloroform ($CH_3CCl_3$) observations. The inverse modeling method optimizes the agreement between model-calculated and observed methane mixing ratios by adjusting the magnitudes of the various methane sources and sinks. The adjustment is constrained by specified a priori estimates and uncertainties of the source and sink magnitudes. We also include data on the $^{13}C/^{12}C$ isotope ratio of atmospheric methane and its sources in the model. Focusing on the 1980s, two scenarios of global methane sources are constructed which reproduce the main features seen in the National Oceanic and Atmospheric Administration's Climate Monitoring and Diagnostics Laboratory (NOAA/CMDL) methane observations. Differences between these two scenarios may probably be attributed to underestimated a priori uncertainties of wetland emissions. Applying the inverse model, the average uncertainty of methane source magnitudes could be reduced by at least one third. We also examined the decrease in the atmospheric methane growth rate during the early 1990s but could not uniquely associate it with changes in particular sources.

## 1. Introduction

Methane ($CH_4$) absorbs infrared radiation at wavelengths around 7.7 $\mu$m and thus plays an important role in the radiative balance of the Earth's atmosphere. The increase in its mean atmospheric mixing ratio from approximately 700 parts per billion by volume (ppbv) in preindustrial times to more than 1700 ppbv today is responsible for roughly 15% of the anthropogenic greenhouse forcing. Since it is predominantly oxidized in a reaction chain initialized by reaction with the hydroxyl (OH) radical, thus providing a major sink for OH, methane also influences atmospheric chemistry. Its accumulation may lead to a long-term reduction of the tropospheric oxidizing capacity. Furthermore, methane also plays an important role in stratospheric chemistry by providing the primary in situ source for water vapor.

The main sources and sinks of atmospheric methane have been identified, but there are still large quantitative uncertainties in the magnitudes of the sources. Improved knowledge about methane sources and sinks is necessary, if we want to determine the most effective ways of reducing methane emissions. The three principal methane producing processes that have been identified are (1) production by bacteria under anaerobic conditions (e.g., in wetlands, rice paddies, in the stomachs of cattle, in landfills), (2) fossil fuel related emissions (coal, oil and natural gas), and (3) incomplete burning

[1]Now at Institut für Physik der Atmosphäre, DLR Oberpfaffenhofen, D-82234 Weßling, Germany.



Paper number 96GB03043.
0886-6236/97/96GB-03043$12.00

of biomass. One way to quantify methane sources is, of course, to perform direct flux measurements in major source regions. Unfortunately, measurements, for example, in wetlands and rice paddies, depend on many meteorological and biological parameters and show a very high variability in space and time. This makes a sound extrapolation from measurements at a few sites to the whole world highly uncertain.

Atmospheric $CH_4$ mixing ratios have been recorded regularly in the global cooperative air sampling network administered by the U.S. National Oceanographic and Atmospheric Administration's Climate Monitoring and Diagnostics Laboratory (NOAA/CMDL) in Boulder, Colorado. Data are available since 1983 and provide an extensive set of measurements of atmospheric methane mixing ratios.

One might ask, whether it is possible to determine global $CH_4$ sources and sinks from these data. An investigation of this question requires a realistic atmospheric transport model which can be run with arbitrary source/sink configurations. The resulting modeled $CH_4$ mixing ratios can then be compared to the observations, and only those source/sink configurations that reproduce the main features seen in the observations will be accepted. Such a study was first carried out by *Fung et al.* [1991] with a three-dimensional atmospheric transport model which was run with seven different source/sink configurations.

In the present study, we used an inverse modeling method which not only allows the selection of the source/sink configuration that gives the best agreement between observed and calculated $CH_4$ mixing ratios but which also enables an objective treatment of the uncertainties of the source and sink magnitudes. Thus it provides information on the extent to which the atmospheric observations constrain the source and sink magnitudes and allows us to determine the range of methane emissions which are consistent with the atmospheric observations. Mathematically, the inverse model constitutes an optimization problem, with the cost function defined as the sum of (weighted) squared deviations of modeled and observed $CH_4$ data. The solution of this optimization problem is given by those source/sink magnitudes that minimize this cost function and lead to an optimal agreement between modeled and observed $CH_4$ data.

In the present study, the geographical and temporal variability of most $CH_4$ sources was chosen in a way similar to *Fung et al.* [1991]. The atmospheric $CH_4$ sink due to reaction with OH radicals is calculated with a chemical module included in the transport model.

Recently, *Brown* [1993, 1995] published a study on inverse methane modeling, following the so-called "total inversion approach," where base source components correspond to the total net emissions from individual latitude bands and are not connected to any particular biogeochemical process. The present study follows the method of "synthesis inversion" [*Enting et al.*, 1993]. Here the different methane emitting processes constitute the base source/sink components. Available information on their temporal and geographical variability is included in the calculations.

This paper is subdivided into three parts. In the first part (section 2), the three-dimensional transport and chemistry model used in this study is described and the calculated OH concentrations obtained with this combined transport-chemistry model are discussed. In the second part (section 3), the calculated OH concentrations are validated, making use of the anthropogenic trace gas methyl chloroform ($CH_3CCl_3$). From this, a uniform global correction factor for the calculated OH concentrations is determined in order to match the observed increase of $CH_3CCl_3$ mixing ratios in the 1980s. The calculated monthly mean OH concentrations are then used in the inverse modeling calculations described in the third part of this study (sections 4–8). Section 4 contains the theoretical background of the inverse modeling method [*Tarantola and Valette*, 1982a, *Tarantola*, 1987]. The statistical data analysis performed with the observational data to be used in the inverse model and the incorporation of isotopic data into the model are described in section 5. In section 6, the base methane source and sink components, their geographical and temporal variation, and the a priori estimated source magnitudes are described. The resulting source and sink estimates obtained from the inverse model as well as the corresponding $CH_4$ mixing ratios and $\delta^{13}CH_4$ isotope ratios are then described in section 7, together with several sensitivity studies. Finally, the conclusions are summarized in section 8.

## 2. Atmospheric Transport and Chemistry Model

### 2.1. Transport Model Description

In the present study, we employed the three-dimensional transport model TM2, developed at the Max-Planck-Institut für Meteorologie in Hamburg, Germany [*Heimann*, 1995]. It numerically solves for an arbitrary number of tracers the continuity equation

$$\frac{d}{dt}\left(\rho(x,t)\chi(x,t)\right) = Q(x,t) \qquad (1)$$

on a global eulerian grid. Here $\rho$ denotes the air density, $\chi$ denotes the tracer's volume mixing ratio, and $Q$ denotes its net sources, all depending on spatial coordinates $x$ and time $t$. The total time derivative operator $d/dt$ describes the different transport processes represented in the model: advection resolved on the model grid and subgridscale vertical transport due to

convective cumulus clouds, vertical turbulence, and dry convection. Atmospheric mass fluxes and subgridscale transport data are based on the 12-hourly meteorological analyses from the European Centre for Medium-Range Weather Forecast (ECMWF) in Reading, England. These data are available with a horizontal resolution of 2.5°×2.5° and on 14 vertical levels. They are interpolated and integrated to yield mass fluxes on the TM2 grid as described by *Heimann and Keeling* [1989] and *Heimann* [1995]. The TM2 model uses the results of this data preprocessing to calculate the three-dimensional advective transport by means of the slopes scheme of *Russell and Lerner* [1981]. Subgridscale vertical transport due to convective clouds is calculated from ECMWF's meteorological analyses using a simplified version of the mass flux scheme of *Tiedtke* [1989]. Turbulent vertical transport is computed by stability-dependent vertical diffusion based on the method described by *Louis* [1979]. The present model version does not contain any explicit horizontal diffusion terms. All calculations for this study were performed with the coarse grid model version (with a horizontal resolution of approximately 8° latitude by 10° longitude and nine vertical levels) and with meteorological data based on the ECMWF analyses for the year 1987, although in one sensitivity study (section 7.2), we used ECMWF's wind data analyses for 1986. The time step for the numerical integration in the model was chosen to be 4 hours. Earlier versions of the model have been described by *Heimann and Keeling* [1989], *Heimann et al.* [1990], and *Brost and Heimann* [1991].

## 2.2. Chemistry Module Description

**2.2.1. Chemical reactions.** The chemical part of the model, developed at the Max-Planck-Institut für Chemie in Mainz, Germany [*Crutzen and Zimmermann*, 1991], describes the tropospheric background $CH_4$ – CO – $O_3$ – $NO_x$ – OH chemistry. In this study, it is used to calculate the large-scale geographical and temporal distribution of OH radicals in the troposphere.

The primary OH production is initialized by the action of solar ultraviolet (UV) radiation on ozone ($O_3$),

$$\text{(R1)} \qquad O_3 \xrightarrow{h\nu} O(^1D) + O_2 \quad (\lambda \leq 320 \text{ nm}).$$

The excited oxygen atoms ($O(^1D)$) may then react with water vapor to form hydroxyl radicals,

$$\text{(R2)} \qquad O(^1D) + H_2O \longrightarrow 2OH,$$

or they are quenched to ground state oxygen atoms (O) which recombine with molecular oxygen ($O_2$) to regenerate ozone,

$$\text{(R3)} \qquad O(^1D) \xrightarrow{M} O \xrightarrow{+O_2} O_3.$$

As a consequence of (R1) to (R3), most OH radicals are formed under warm and humid conditions and high intensities of UV radiation. Because hydroxyl radicals are highly reactive, they initialize the oxidation of many trace gases emitted into the atmosphere by natural or anthropogenic processes and are thus sometimes called the "detergent" of the atmosphere.

Most OH radicals react with CO, $CH_4$, or methane's oxidation products. Carbon monoxide (CO) is oxidized to give carbon dioxide ($CO_2$),

$$\text{(R4)} \qquad CO + OH \xrightarrow{+O_2} CO_2 + HO_2.$$

In a $NO_x$-rich environment, this reaction is usually followed by

$$\text{(R5)} \qquad NO + HO_2 \longrightarrow NO_2 + OH$$

and

$$\text{(R6)} \qquad NO_2 \xrightarrow{h\nu,O_2} NO + O_3 \quad (\lambda \leq 420 \text{ nm})$$

which results in net ozone production. Under $NO_x$-poor conditions, however,

$$\text{(R7)} \qquad O_3 + HO_2 \longrightarrow OH + 2O_2$$

primarily takes place, leading to a net ozone destruction. During daytime, the lifetime of the nitrogen oxides is determined by the reactions

$$\text{(R8)} \qquad NO + O_3 \longrightarrow NO_2 + O_2$$

and

$$\text{(R9)} \qquad NO_2 + OH \xrightarrow{M} HNO_3,$$

followed by removal of $HNO_3$ from the atmosphere by wet or dry deposition. A lesser fraction may also react with OH,

$$HNO_3 + OH \longrightarrow H_2O + NO_3$$

$$\text{(R10)} \qquad \xrightarrow{h\nu,O_2} H_2O + NO_2 + O_3,$$

or be photolyzed,

$$\text{(R11)} \qquad HNO_3 \xrightarrow{h\nu} NO_2 + OH \quad (\lambda \leq 320 \text{ nm}),$$

giving back $NO_x$. At nighttime, the formation of $NO_3$ and $N_2O_5$ also play a significant role in $NO_x$ loss. $NO_3$ is produced by

$$\text{(R12)} \qquad NO_2 + O_3 \longrightarrow NO_3 + O_2.$$

During daytime, it is rapidly photolyzed without any net effect, but during nighttime, $N_2O_5$ molecules can be formed by

(R13) $NO_3 + NO_2 \longrightarrow N_2O_5$.

In remote areas, most of these $N_2O_5$ molecules (in the model approximately 70%) will decay and give back $NO_2$ and $NO_3$,

(R14) $N_2O_5 \longrightarrow NO_2 + NO_3$,

again without any net effect. However, in more polluted areas, the $N_2O_5$ molecules can produce $HNO_3$ by heterogenous processes on wet aerosol surfaces,

(R15) $N_2O_5 + H_2O \longrightarrow 2HNO_3$,

thus leading to $NO_x$ destruction. The effect of this nighttime $NO_x$ removal was included in the present model version in a parameterized way: The probability for each $N_2O_5$ molecule to form $HNO_3$ by (R15) before it decays (R14) was calculated with the three-dimensional global atmospheric model MOGUNTIA [*Dentener and Crutzen*, 1993; *Dentener*, 1993]. These geographically and monthly varying probabilities were used in this study to calculate the conversion rates from $NO_x$ to $HNO_3$ by (R15).

The methane oxidation scheme is more complex but similar to that of carbon monoxide. It is also initialized by the reaction with an OH radical,

(R16) $CH_4 + OH \longrightarrow CH_3 + H_2O \xrightarrow{+O_2} CH_3O_2 + H_2O$.

If enough $NO_x$ is present, this reaction is followed by

(R17) $CH_3O_2 + NO \xrightarrow{+O_2} CH_2O + NO_2 + HO_2$,

and $NO_2$ photolysis (R6), leading to net ozone production. In the $NO_x$-poor parts of the atmosphere,

(R18) $CH_3O_2 + HO_2 \longrightarrow CH_3O_2H + O_2$,

followed by

(R19) $CH_3O_2H + OH \longrightarrow CH_2O + OH + H_2O$

or by

$$CH_3O_2H \xrightarrow{h\nu} CH_3O + OH$$

(R20) $\xrightarrow{+O_2} CH_2O + HO_2 + OH \quad (\lambda \leq 370 \text{ nm})$,

takes place, leading to $CH_2O$ without chemical ozone formation. The reaction

(R21) $CH_3O_2H + OH \longrightarrow CH_3O_2 + H_2O$,

together with (R18), forms a catalytic cycle which destroys OH and $HO_2$. Formaldehyde ($CH_2O$) further reacts with OH,

(R22) $CH_2O + OH \xrightarrow{+O_2} CO + HO_2 + H_2O$,

or is photolyzed,

(R23) $CH_2O \xrightarrow{h\nu} CO + H_2 \quad (\lambda \leq 365 \text{ nm})$,

or

$$CH_2O \xrightarrow{h\nu} CHO + H$$

(R24) $\xrightarrow{+2O_2} CO + 2HO_2 \quad (\lambda \leq 330 \text{ nm})$.

All these reactions result in CO formation. CO will further be oxidized to $CO_2$ as described above. Some additional reactions which influence the budgets of OH and $HO_2$ radicals are also taken into account in the present model:

(R25) $HO_2 + HO_2 \longrightarrow H_2O_2 + O_2$,

(R26) $H_2O_2 \xrightarrow{h\nu} 2OH \quad (\lambda \leq 355 \text{ nm})$,

(R27) $H_2O_2 + OH \longrightarrow HO_2 + H_2O$,

(R28) $O_3 + OH \longrightarrow HO_2 + O_2$,

and

(R29) $HO_2 + OH \longrightarrow H_2O + O_2$.

The reaction rates used in the model have been taken from the Jet Propulsion Laboratory (JPL) data compilation [*DeMore et al.*, 1992] and are listed in Table 1. Photolysis rates have been calculated with a two-dimensional photochemical model [*Brühl and Crutzen*, 1993] using zonal mean cloud statistics and their model-calculated stratospheric ozone concentrations. They are averaged over time periods of 2 weeks. The recent findings concerning quantum yields of ozone leading to higher $O(^1D)$ and OH production than previously calculated [*Michelsen et al.*, 1994] have been taken into account. The time step for the numerical integration of the chemical transformations of trace gases in the model, as well as for emissions and deposition, was set to 2 hours, which is half of the transport integration time step.

**2.2.2. Emissions.** Surface emissions of $NO_x$ from soils, biomass burning, and industry are included in the model (Table 2). In the middle and upper troposphere, lightning constitutes the most important $NO_x$ source. Aircraft emissions and transport of $NO_x$ from the stratosphere into the troposphere are neglected in the present study. The geographical distribution of the $NO_x$ emissions from industrial sources and biomass burning have been taken from the data compilations of C. M. Benkovitz et al. (manuscript in preparation, 1996) and *Hao et al.* [1990], respectively. The emissions from biomass burning are given on a monthly ba-

**Table 1.** Photochemical Reactions and Rate Constants Used In the Tropospheric Chemistry Module

| | Reaction | | Rate constant, $cm^3s^{-1}$ |
|---|---|---|---|
| (R1) | $O_3$ | $\xrightarrow{h\nu} O(^1D) + O_2$ | |
| (R2) | $O(^1D) + H_2O$ | $\longrightarrow 2OH$ | $2.2 \times 10^{-10}$ |
| (R3) | $O(^1D)$ | $\xrightarrow{M} O \xrightarrow{+O_2} O_3$ | $3.2 \times 10^{-11} \times e^{70K/T} \times 0.2095 \times M$ $+1.8 \times 10^{-11} \times e^{110K/T} \times 0.781 \times M$ |
| (R4) | $CO + OH$ | $\xrightarrow{+O_2} CO_2 + HO_2$ | $1.5 \times 10^{-13} \times (1 + 0.6p)$ |
| (R5) | $NO + HO_2$ | $\longrightarrow NO_2 + OH$ | $3.7 \times 10^{-12} \times e^{250K/T}$ |
| (R6) | $NO_2$ | $\xrightarrow{h\nu,O_2} NO + O_3$ | |
| (R7) | $O_3 + HO_2$ | $\longrightarrow OH + 2O_2$ | $1.1 \times 10^{-14} \times e^{-500K/T}$ |
| (R8) | $NO + O_3$ | $\longrightarrow NO_2 + O_2$ | $2 \times 10^{-12} \times e^{-1400K/T}$ |
| (R9) | $NO_2 + OH$ | $\xrightarrow{M} HNO_3$ | $k_{NO_2,OH}$ |
| (R10) | $HNO_3 + OH$ | $\longrightarrow H_2O + NO_3$ | $k_{HNO_3,OH}$ |
| | | $\xrightarrow{h\nu,O_2} H_2O + NO_2 + O_3$ | |
| (R11) | $HNO_3$ | $\xrightarrow{h\nu} NO_2 + OH$ | |
| (R16) | $CH_4 + OH$ | $\longrightarrow CH_3 + H_2O \xrightarrow{+O_2} CH_3O_2 + H_2O$ | $2.9 \times 10^{-12} \times e^{-1820K/T}$ |
| (R17) | $CH_3O_2 + NO$ | $\xrightarrow{+O_2} CH_2O + NO_2 + HO_2$ | $4.2 \times 10^{-12} \times e^{180K/T}$ |
| (R18) | $CH_3O_2 + HO_2$ | $\longrightarrow CH_3O_2H + O_2$ | $3.8 \times 10^{-13} \times e^{800K/T}$ |
| (R19) | $CH_3O_2H + OH$ | $\longrightarrow CH_3O_2 + H_2O$ | $3.8 \times 10^{-12} \times e^{200K/T} \times 70\%$ |
| (R20) | $CH_3O_2H$ | $\xrightarrow{h\nu} CH_3O + OH$ | |
| | | $\xrightarrow{+O_2} CH_2O + HO_2 + OH$ | |
| (R21) | $CH_3O_2H + OH$ | $\longrightarrow CH_2O + OH + H_2O$ | $3.8 \times 10^{-12} \times e^{200K/T} \times 30\%$ |
| (R22) | $CH_2O + OH$ | $\xrightarrow{+O_2} CO + HO_2 + H_2O$ | $1 \times 10^{-11}$ |
| (R23) | $CH_2O$ | $\xrightarrow{h\nu} CO + H_2$ | |
| (R24) | $CH_2O$ | $\xrightarrow{h\nu} CHO + H \xrightarrow{+2O_2} CO + 2HO_2$ | |
| (R25) | $HO_2 + HO_2$ | $\longrightarrow H_2O_2 + O_2$ | $k_{HO_2,HO_2}$ |
| (R26) | $H_2O_2$ | $\xrightarrow{h\nu} 2OH$ | |
| (R27) | $H_2O_2 + OH$ | $\longrightarrow HO_2 + H_2O$ | $2.9 \times 10^{-12} \times e^{-160K/T}$ |
| (R28) | $O_3 + OH$ | $\longrightarrow HO_2 + O_2$ | $1.6 \times 10^{-12} \times e^{-940K/T}$ |
| (R29) | $HO_2 + OH$ | $\longrightarrow H_2O + O_2$ | $4.8 \times 10^{-11} \times e^{250K/T}$ |

$$k_{HO_2,HO_2} = (2.3 \times 10^{-13} e^{600K/T} + 1.7 \times 10^{-33} cm^3 e^{1000K/T} M)(1 + 1.4 \times 10^{-21} cm^3 e^{2200K/T} [H_2O]) cm^3 s^{-1}$$

$$k_{NO_2,OH} = \frac{k_0(T) \times M \times k_\infty(T)}{k_0(T) \times M + k_\infty(T)} \times 0.6^{\left(1 + \left(\log_{10} \frac{k_0(T) \times M}{k_\infty(T)}\right)^2\right)^{-1}}$$

with

$$k_0(T) = 2.6 \times 10^{-30} \times \left(\frac{T}{300K}\right)^{-3.2} cm^6 s^{-1} \text{ and } k_\infty(T) = 2.4 \times 10^{-11} \times \left(\frac{T}{300K}\right)^{-1.3} cm^3 s^{-1}$$

$$k_{HNO_3,OH} = \left(7.2 \times 10^{-15} \times e^{785K/T} + \frac{4.1 \times 10^{-16} \times e^{1440K/T} \times 1.9 \times 10^{-33} e^{725K/T} \times M}{4.1 \times 10^{-16} \times e^{1440K/T} + 1.9 \times 10^{-33} e^{725K/T} \times M}\right) cm^3 s^{-1}$$

Rate constants [*DeMore et al.*, 1992] are in cubic centimeters per second. $T$, absolute Temperature (Kelvin), $p$, air pressure (atmospheres), $M$, air density (per cubic centimeter).

sis. However, it is important to note that their temporal variation is relatively uncertain. There are no indications that industrial $NO_x$ emissions have a substantial seasonal variation. In the model, they are thus assumed to be constant throughout the year.

In agreement with *Crutzen and Zimmermann* [1991], $NO_x$ emissions from soils are parameterized using a simple temperature dependence and taking into account that no $NO_x$ is emitted from frozen soils and deserts. With $\vartheta$ being the local monthly mean surface air temperature in degrees Celsius, $NO_x$ fluxes per area land surface are assumed to be proportional to $\vartheta + 5$. Deserts are characterized by $p \leq 2\vartheta$, where p denotes the local monthly precipitation in millimeters, and soils are assumed to be frozen if the local monthly mean surface air temperature falls below −5°C. In agreement with *Dentener and Crutzen* [1993], the global annual magnitude of $NO_x$ emissions from soils was set to 4 Tg N.

The global magnitude of the $NO_x$ emissions from lightning is highly uncertain. *Logan* [1983] estimated a range of 2–20 Tg/yr N, and even up to 100 Tg/yr N have been suggested [*Franzlau and Popp*, 1989]. We de-

**Table 2.** Characterization of Atmospheric Sources of Nitrogen Oxides

| Source | Global Magnitude | Spatial Variation | Temporal Variation | Reference |
|---|---|---|---|---|
| Industrial | 22.2 Tg/yr N | in industrial areas (predominantly eastern United States, central Europe, and Japan) | none | C. M. Benkovitz et al., (manuscript in preparation, 1996) |
| Soils | 4 Tg/yr N | predominantly over tropical land (except deserts) | temperature and precipitation dependent | *Crutzen and Zimmermann* [1991] and *Dentener and Crutzen* [1993] |
| Biomass Burning | 5 Tg/yr N | mainly between 25°N and 25°S | in dry season | *Hao et al.* [1990] |
| Lightning | 9.9 Tg/yr N | in middle and upper troposphere; enhanced over tropics, lower over sea | depending on convective activity | *Price and Rind* [1994] |
| Flux from the stratosphere | neglected | | | |
| Aircraft | neglected | | | |

scribed its geographical and temporal distribution according to a parametrization recommended by *Price and Rind* [1992, 1994] which empirically relates flash frequencies to convective cloud top heights and distinguishes between continental and marine conditions. To calculate $NO_x$ emissions, a globally uniform $NO_x$ production of $2 \times 10^{25}$ molecules per flash was assumed [*Lawrence et al.*, 1995]. This parametrization led to a global $NO_x$ lightning source magnitude of 9.9 Tg/yr N.

Because the surface emissions for $CH_4$ and CO are not well established, we specified measured surface mixing ratios rather than emissions. For methane, these are based on results obtained with a preliminary version of the inverse model described in this paper [*Hein*, 1994], and for CO from the latitude-time distributions given by *Dianov-Klokov and Yurganov* [1981] and *Dianov-Klokov et al.* [1989]. Since CO emissions primarily take place over continents, we assumed, as a rough estimate, CO surface mixing ratios over continents to be 40% higher than over sea at the corresponding latitude. We are aware of the fact that this is a rather simple assumption. With more atmospheric CO measurements becoming available, a more detailed treatment of the global CO cycle in global chemical models should be possible. This might alter the geographical and temporal distribution of model-calculated OH concentrations.

**2.2.3. Ozone flux from the stratosphere.** Because the amount of ozone that crosses the tropopause is highly uncertain, and since the model, due to its coarse resolution, is not able to calculate cross-tropopause fluxes of air masses in a realistic way, we prescribed ozone mixing ratios at the uppermost tropospheric model level (in tropics, model level 7, centered at 200 hPa, and in nontropical regions, model level 6, centered at 320 hPa) according to climatological ozone data derived from ozonesonde measurements [*Fortuin and Langematz*, 1994]. It is important to note that due to the inhomogeneous distribution of ozonesonde stations, the accuracy of the climatology is highest in the midlatitudes of the northern hemisphere and lowest in the equatorial region and in the midlatitudes of the southern hemisphere.

**2.2.4. Wet deposition.** According to *Junge and Gustafson* [1957], wet deposition causes a change in the concentration C of a species that can be expressed by

$$\frac{\partial C}{\partial t} = -L_k C \tag{2}$$

with the deposition rate $L_k$ given by

$$L_k = \frac{\epsilon P}{\Delta z_k L}. \tag{3}$$

$P$ denotes the precipitation rate which originates from the corresponding layer, calculated from ECMWF's daily precipitation forecasts [*Arpe*, 1991] and a climatological vertical distribution of precipitation formation [*Newell et al.*, 1974], $\Delta z_k$ denotes the thickness of the model layer, and $L$ denotes the volume fraction of liquid water in clouds, defined as the ratio of the liquid water content (LWC) of the rain-producing cloud and the specific weight of water ($10^6$ gm$^{-3}$). Assuming a globally uniform LWC of 1 gm$^{-3}$, we obtain $L = 10^{-6}$. The scavenging efficiency $\epsilon$ can be approximated by the equilibrium ratio of water dissolved to total trace gas mass. Following Henry's law, this ratio can be calculated by

$$\epsilon = \frac{LHRT}{1 + LHRT} \tag{4}$$

where $R$ denotes the universal gas constant, $T$ denotes the temperature, and $H$ denotes the Henry constant of the trace gas. This parametrization neglects below-cloud scavenging and does not separate between con-

**Table 3.** Henry Constants

| Species | Henry Constant |
|---|---|
| $H_2O_2$ | $1.67 \times 10^{-5} \times e^{6621K/T}$ |
| $CH_3O_2$ | $1.5 \times 10^{-6} \times e^{5607K/T}$ |
| $HNO_3$ | so highly soluble that $\epsilon = 1$ can be assumed |

Henry constants are in mole per liter and per atmosphere

vective and stratiform precipitation. Values for Henry constants [*Lind and Kok*, 1986] used in this study are given in Table 3.

**2.2.5. Dry deposition.** Dry deposition can remove $O_3$, $NO_x$, $H_2O_2$, $CH_3O_2H$, and $HNO_3$ from the surface layer of the atmosphere. The trace gas flux $F$ to the surface is usually described as a first-order loss process; that is, $F$ is the product of the trace gas concentration $C$ and a depostion velocity $v$,

$$F = vC. \tag{5}$$

With one exception, the deposition velocities used in the model are based on measurements from *Wesely* [1989] and *Galbally and Roy* [1980] and are similar to the values used by *Valentin* [1990] and *Dentener and Crutzen* [1993]. The exception refers to ozone: On the basis of measurements by *Kawa and Pearson* [1989], a much lower ozone deposition velocity over sea of 0.25 mm/s compared to earlier estimates of 1 mm/s was applied. To correct for lower values of the concentration of species deposited at the surface compared to the center of the lowest model grid box, the deposition velocity is multiplied with a wind speed dependent correction factor

$$\frac{c_D v_{\text{wind}}}{v + c_D v_{\text{wind}}}, \tag{6}$$

as recommended by *Levy and Moxim* [1989]. Here $c_D$ denotes a drag coefficient, taken to be 0.002 globally, and $v_{\text{wind}}$ is the absolute local horizontal wind speed in the bottom model layer. See *Levy et al.* [1985] for more details.

### 2.3. Calculated OH Radical Concentration

Figures 1 and 2 show the calculated OH radical concentration in January and July.

Zonal mean concentrations are very similar to those calculated by *Spivakovsky et al.* [1990] and *Dentener and Crutzen* [1993]. They peak in the tropical free troposphere between approximately 400 and 800 hPa. Largely following the Sun's seasonal position, concentrations are highest around 20°S in January and around 30°N in July. Because of higher $NO_x$ and $O_3$ concentrations in the northern hemisphere, the northern summer maximum is stronger than in the southern hemisphere.

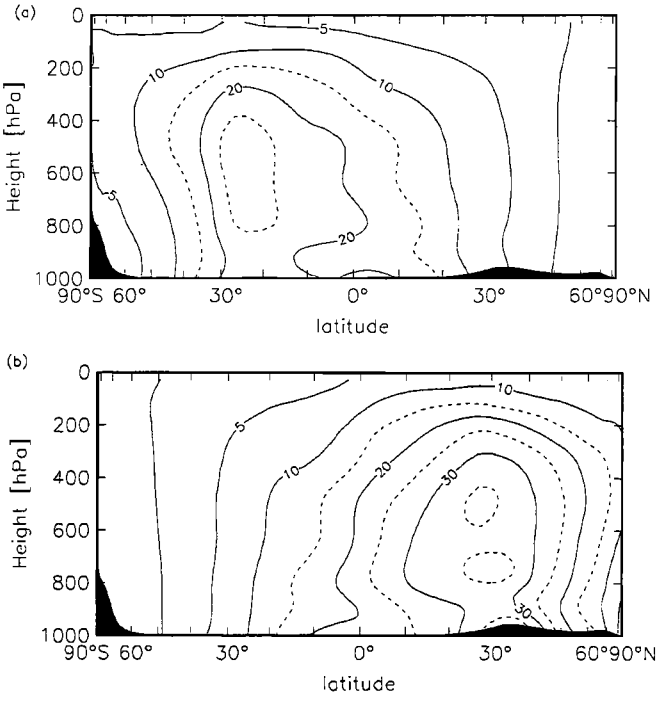


**Figure 1.** Simulated monthly and zonal mean OH concentrations in a) January and b) July; unit: $10^5 cm^{-3}$ (24-hour mean values).

As shown in Figure 2, OH concentrations over continents are in most cases much higher than in oceanic regions. This can again be attributed mainly to differences in $NO_x$ concentrations: Since $NO_x$ is emitted mainly over continents and has a short lifetime of few days, its concentrations rapidly decrease by several orders of magnitude in remote regions. $NO_x$ concentrations strongly influence OH concentrations by two mechanisms. First, ozone concentrations are usually enhanced in $NO_x$-rich regions due to the ozone formation from $NO_2$ photolysis (R6). This directly translates into enhanced OH production via (R1) and (R2). Second, $HO_2$ radicals which are formed during the oxidation of CO (R16) as well as during $CH_4$ oxidation (R17, R22, and R24) are converted into OH radicals by reaction with NO or $O_3$. Since the reaction of $HO_2$ with NO (R5) is much faster than with $O_3$ (R7), this OH recycling is much more efficient in $NO_x$-rich parts of the atmosphere where it can significantly exceed the "primary" OH production by reaction of $O(^1D)$ with water vapor (R2).

## 3. Methyl Chloroform Modeling to Check Calculated OH Concentrations

Methyl chloroform (1,1,1-Trichloroethane, $CH_3CCl_3$) is a chemical of purely anthropogenic origin. Its sources to the atmosphere are relatively well known

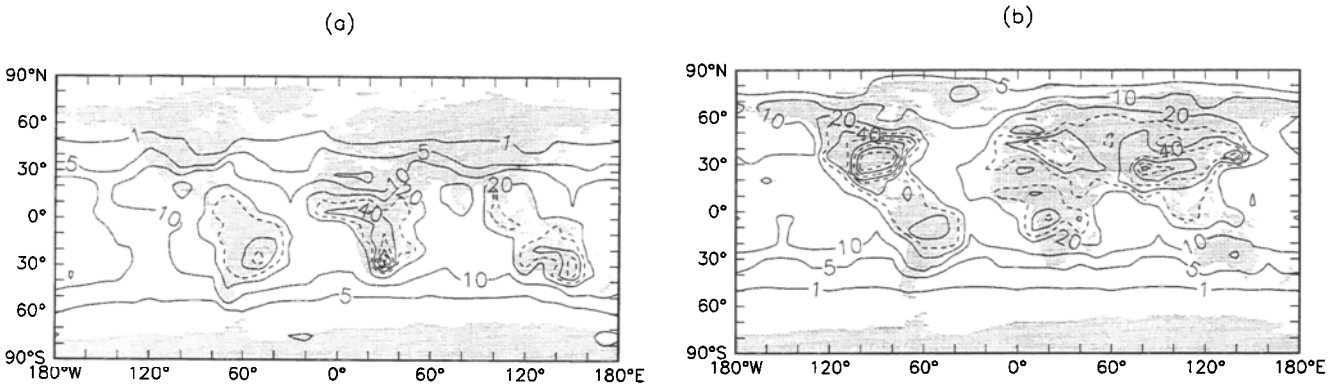


**Figure 2.** Simulated monthly mean OH concentrations in model level 1 (surface) in a) January and b) July; unit: $10^5 cm^{-3}$ (24-hour mean values).

from production figures reported by the chemical industry [*Prinn et al.*, 1992; *Midgley*, 1989]. Following *Kanakidou et al.* [1995], $CH_3CCl_3$ emissions for 1986 reported for five regional areas [*Midgley and McCulloch*, 1995] were distributed among the countries within each region proportional to their CFC-113 production figures [*McCulloch et al.*, 1994]. Within each country, constant per capita emissions were assumed. The dominant sink of $CH_3CCl_3$ is reaction with OH radicals,

(R30) $\quad CH_3CCl_3 + OH \longrightarrow CH_2CCl_3 + H_2O.$

Its atmospheric concentrations have been regularily recorded since the end of the 1970s at five stations during the Atmospheric Lifetime Experiment/Global Atmospheric Gases Experiment (ALE/GAGE) [*Prinn et al.*, 1992]. It is important to note that the earlier absolute calibration of the ALE/GAGE $CH_3CCl_3$ measurements [*Prinn et al.*, 1992] has recently been revised [*Prinn et al.*, 1995], leading to approximately 20% smaller concentrations and thus a correspondingly shorter $CH_3CCl_3$ lifetime. Consequently, the estimated global averaged OH concentration as calculated by optimally fitting the observed increase in $CH_3CCl_3$ mixing ratios has increased by 20% [*Prinn et al.*, 1995]. Two relatively minor methyl chloroform loss processes are photolysis in the stratosphere and hydrolysis in the ocean [*Butler et al.*, 1991]. Photolysis in the stratosphere was included in the model based on calculations with a two-dimensional photochemical model [*Brühl and Crutzen*, 1993], yielding a calculated effective global lifetime of $CH_3CCl_3$ due to stratospheric loss of 44 years. Assuming that $CH_3CCl_3$ concentrations in the upper oceanic layer are in Henry's law equilibrium with the atmosphere, the $CH_3CCl_3$ flux from the atmosphere to the ocean was calculated with a three-dimensional oceanic general circulation model [*Maier-Reimer*, 1993; *Maier-Reimer et al.*, 1993] that includes hydrolysis. The calculated atmospheric lifetime of methyl chloroform due to the oceanic sink is 106 years, approximately 20% higher than estimated by *Butler et al.* [1991]. Since oceanic uptake contributes with less than 10% to all $CH_3CCl_3$ sinks, the estimated global averaged OH concentration is not very sensitive to errors in this sink and would be only 1-2% higher if the higher ocean sink estimated by *Butler et al.* [1991] were used. Hence potential errors in the applied hydrolysis rate and Henry's law constant, even though both have a high relative uncertainty [*Butler et al.*, 1991; *Gossett*, 1987; *Jeffers et al.*, 1989], are of minor importance for the global $CH_3CCl_3$ cycle.

We run the three-dimensional transport model TM2 with $CH_3CCl_3$ sources and sinks as described above. The applied OH concentrations were taken from the coupled transport-chemistry model and multiplied with a uniform global correction factor $\alpha_{OH}$. The methyl chloroform concentrations obtained with the model were then compared with the observations at the ALE/GAGE stations taking into account the revised absolute calibration of the $CH_3CCl_3$ measurements. This provides a check on the globally integrated calculated OH concentrations. An optimal agreement (minimized root mean squared deviation) between modeled and observed methyl chloroform mixing ratios was achieved with a uniform global correction factor for the precalculated OH concentrations of 0.82. The mathematical procedure to determine this optimal value for $\alpha_{OH}$ is described in more detail by Hein [1994].

The corrected tropospheric annual and 24-hour mean OH concentration, weighted by pressure and the temperature dependence of the $CH_3CCl_3$ + OH reaction, is $10.3 \times 10^5$ $cm^{-3}$, towards the upper edge of the range of $9.7 \pm 0.6 \times 10^5$ $cm^{-3}$ calculated by *Prinn et al.* [1995]. The corresponding tropospheric methyl chloroform lifetime due to OH reaction is 5.1 years, within the range of $4.9 \pm 0.3$ years estimated by *Prinn et al.* [1995] based on a 12-box global atmospheric model. The reason why *Prinn et al.* [1995] obtain a slightly lower lifetime despite lower annual mean OH concentrations is not clear.

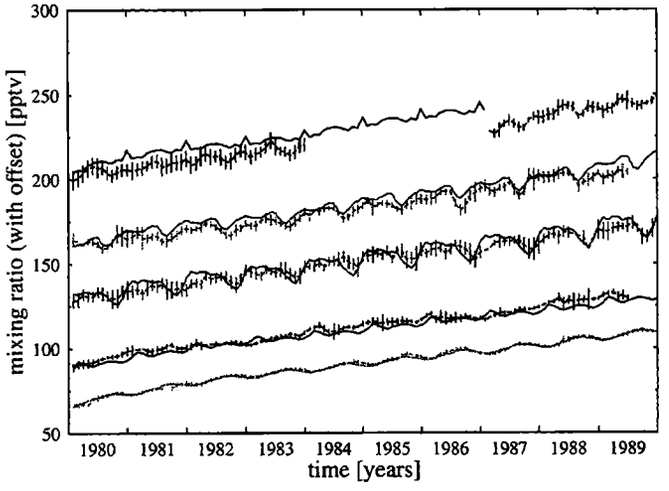


**Figure 3.** The model-calculated increase in atmospheric $CH_3CCl_3$ mixing ratios (solid lines) compared to ALE/GAGE observations [*Prinn et al.*, 1992, 1995] (dashed lines with errorbars (mean variation within each month)) during the 1980s. Offset for plotting the values for Adrigole/Mace Head (Ireland), Cape Meares (Oregon), Ragged Point (Barbados), Matatula Point (American Samoa), and Cape Grim (Tasmania) was 100, 60, 40, 20, and 0 parts per trillion by volume (pptv), respectively.

It is probably attributed to a different description of $CH_3CCl_3$ emissions, transport, and sinks (in particular differences in the applied stratospheric loss rates) and the very different horizontal, vertical, and temporal resolutions of the two models.

The $CH_4$ lifetime is approximately 1.6 times greater than the lifetime of $CH_3CCl_3$ due to its slower reaction with OH. With the TM2 model, we obtain a tropospheric methane lifetime due to reaction with OH of 8.3 years. This value is also in the upper part of the range of 8.0 $\pm$ 0.5 years estimated by *Prinn et al.* [1995].

The time series of the methyl chloroform mixing ratios at the ALE/GAGE stations calculated in the model and the atmospheric observations are shown in Figure 3. It can be seen that the seasonal cycle is generally well reproduced. It should be noted, however, that the two northern midlatitude stations in Ireland (53°N) and Oregon (45°N) are located within model grid boxes in which $CH_3CCl_3$ emissions take place. Consequently, the modeled $CH_3CCl_3$ mixing ratios at these grid points are, in contrast to the observations, not representative for unpolluted air. For these two cases, we therefore used model results taken at the next gridbox west of the stations. The seasonal cycle in Barbados (13°N) is strongly influenced by variations in the location of the Intertropical Convergence Zone (ITCZ). The overall good agreement in Barbados indicates that the ITCZ is, at least in the Caribbean region, reasonably represented in the model. The methyl chloroform mixing ratios in Samoa (14°S) are well reproduced by the model. During El Niño events, however, the observations show an irregular seasonality [*Prinn et al.*, 1992] that cannot be reproduced by the model.

Figure 3 also indicates that the model slightly overestimates the interhemispheric gradient in $CH_3CCl_3$ mixing ratios. Defining the interhemispheric gradient as the difference between the mixing ratios at the ALE/GAGE stations in Oregon (45°N) and Tasmania (41°S), this overestimation amounts to 12%. It may be explained by a small underestimation of interhemispheric transport in the model which has already been detected in a CFC-11 ($CFCl_3$) tracer study [*Hein*, 1994]. Additionally, any underestimation of the fraction of southern hemispheric $CH_3CCl_3$ emissions would also contribute to the overestimated interhemispheric gradient in the model. Therefore, no significant deviation from the modeled OH distribution is required to explain the differences in the modeled latitudinal distribution of $CH_3CCl_3$ mixing ratios compared to the ALE/GAGE observations.

## 4. Inverse Methane Modeling

### 4.1. Inverse Modeling Approach

With an inverse modeling approach based on the method of *Tarantola and Valette* [1982a], we investigated the extent to which the global magnitude of the various methane sources can be constrained by atmospheric observations. This inverse modeling approach was originally applied in geophysics to localize earthquake centers. In atmospheric science, *Enting* [1993] and *Enting et al.* [1993] first used it to study the atmospheric $CO_2$ cycle.

The inversion method adopted in the present study includes a priori information on the observed atmospheric methane mixing ratios and isotope ratios at the monitoring sites in conjunction with a priori estimates of the global magnitudes of individual methane sources and their uncertainties. Thereby the individual base source/sink components are described by their geographical and temporal pattern which is not subject to the optimization but prescribed according to available information as described in sections 6.1 and 6.3. Solving the inverse problem results in a posteriori estimates of methane source magnitudes and their a posteriori uncertainties [*Tarantola and Valette*, 1982a, 1982b; *Tarantola*, 1987]. A significant reduction in the uncertainty of a particular source can be interpreted as indicating that the observational data indeed constrain the magnitude of this source, assuming that the transport model is correct. On the other hand, if the a posteriori uncertainty of a particular source is not much smaller than its a priori uncertainty, then it is implied that this source cannot be resolved by the observational network. This is the case when the atmospheric signal (the contribu-

tion of this source to the spatial and temporal variation in atmospheric $CH_4$ mixing ratios) at the observational sites does not significantly differ from the atmospheric signal of another source or a linear combination of other sources and sinks. The specified a priori estimate of the uncertainty in the magnitude of a particular source also plays an important role. The smaller the assigned uncertainty, the more difficult it is to gain further information from the available observational data. Conversely, it is easier to constrain the more uncertain source magnitudes by inverse modeling than those that are already well established.

In this study, we always assume a quasi-stationary state of the global $CH_4$ cycle; that is, we assume an average state over a target time period of several years (section 5.1), during which no interannual changes in methane sources and sinks are allowed. In contrast to a totally stationary state, however, the observed overall global increase in the atmospheric methane mixing ratio is taken into account.

### 4.2. Modeling Technique

The continuity equation (1) for atmospheric methane may be written in the form

$$T[\rho(x,t)\chi_{\text{model}}(x,t)] = -\lambda_{\text{OH}}(x,t)\rho(x,t)\chi_{\text{model}}(x,t) + \sum_{j=1}^{n} Q_j(x,t), \quad (7)$$

where $x$ denotes the three-dimensional space and $t$ denotes the time coordinate, $j$ runs over all $n$ methane sources $Q_j$, $T$ denotes the operator describing all model transport terms, $\rho$ denotes the air density, $\chi_{\text{model}}$ denotes the modeled methane mixing ratio, and $\lambda_{\text{OH}}$ denotes the rate of methane destruction due to reaction with OH radicals. In this representation, the sink terms due to soil uptake and stratospheric loss are formally included as negative source terms. Approximating $\chi_{\text{model}}$ in the OH sink term with the methane mixing ratio $\chi$ derived from the coupled transport-chemistry model (section 2.2) makes the OH term in equation (7) independent of the model solution $\chi_{\text{model}}$. For convenience, the abbreviation

$$Q_0(x,t) = -\lambda_{\text{OH}}(x,t)\rho(x,t)\chi_{\text{model}}(x,t) \quad (8)$$

is introduced, and for each $j$, a normalized base source component $\hat{Q}_j$ with a global magnitude of unity is defined by

$$\hat{Q}_j(x,t) = \frac{1}{\alpha_j} Q_j(x,t), \quad (9)$$

where the parameters $\alpha_j$ represent the global source magnitudes. Equation (7) can now be written in the form

$$T[\rho(x,t)\chi_{\text{model}}(x,t)] = \sum_{j=0}^{n} \alpha_j \hat{Q}_j(x,t), \quad (10)$$

where the right side is independent of $\chi_{\text{model}}$. Thus the solution $\chi_{\text{model}}$, representing the modeled $CH_4$ mixing ratio, can be expressed as a linear combination

$$\chi_{\text{model}}(x,t) = \sum_{j=0}^{n} \alpha_j \chi_j(x,t) + \alpha_{00}\chi_{00}(x,t) \quad (11)$$

of the solutions $\chi_j$ of the inhomogenous equations

$$T[\rho(x,t)\chi_j(x,t)] = \hat{Q}_j(x,t) \text{ with } \chi_j(x,0) = 0, \quad (12)$$

representing the contributions of the different $CH_4$ sources to the total modeled $CH_4$ mixing ratio and the solution $\chi_{00}$ of the homogenous equation

$$T[\rho(x,t)\chi_{00}(x,t)] = 0 \quad \text{with} \quad \chi_{00}(x,0) = 1, \quad (13)$$

representing the initialization of the model with a globally uniform methane mixing ratio of $\alpha_{00}$. Since mixing ratios are conserved by transport processes, the latter equation has the trivial solution of unity, $\chi_{00}(x,t) = 1$. As described in the Appendix, the $^{13}C/^{12}C$ isotope ratio can, with some approximations, be treated in an analogous way [*Hein and Heimann*, 1993].

To obtain the solutions $\chi_j$, the transport model TM2 is run for 4 years for each source and sink separately. The first 3 years of each run are ignored, and only the fourth year is used. This spin-up time of 3 years is long compared to timescales typical for atmospheric mixing, in particular the interhemispheric exchange time. Hence the gradients in resulting atmospheric methane mixing ratios are largely independent of initial conditions. Possible errors resulting from the initialization with a globally uniform $CH_4$ mixing ratio and a globally constant $\delta^{13}CH_4$ isotope ratio are thus negligible.

### 4.3. Inverse Problem as Least-Squares Optimization

Mathematically, the inversion procedure consists of determining the parameters $\alpha_j$ ($j = 0, \ldots, n$) and $\alpha_{00}$ in order to get an optimal agreement of the model solution $\chi_{\text{model}}$ with a chosen set of observations $\chi_{\text{obs}}$, taking into account the a priori information on the parameters $\alpha_{ap,j}$; that is, to minimize the weighted sum of squared deviations

$$\Delta = \sum_{i=1}^{n_i+2} s_i^{-2} \left(\chi_{\text{model},i} - \chi_{\text{obs},i}\right)^2 + \sum_{j=1}^{n_j} \tilde{s}_j^{-2} \left(\alpha_j - \alpha_{\text{ap},j}\right)^2 . \quad (14)$$

Here $i$ runs over all observational data points in time

and space, $\chi_{\mathrm{model},i}$ and $\chi_{\mathrm{obs},i}$ are the modeled and observed methane mixing ratios at these points, and $j$ runs over all methane sources and sinks, with $\alpha_j$ being the a posteriori and $\alpha_{\mathrm{ap},j}$ being the a priori source/sink magnitude estimates. The term $s_i$ denotes the uncertainty assigned to $\chi_{\mathrm{obs},i}$, and $\tilde{s}_j$ denotes the uncertainty of $\alpha_{\mathrm{ap},j}$. The global mean increase in $CH_4$ mixing ratios and isotope ratios are two additional observational features which are used to constrain the methane source and sink magnitudes. They are formally treated as two additional data points (with indices $n_i + 1$ and $n_i + 2$) and thus included in the summation over $i$. We have (in the base scenario) 22 NOAA/CMDL stations with $CH_4$ measurements and 3 stations with $\delta^{13}CH_4$ measurements with 12 calendar months each; hence $n_i = (22 + 3) \times 12 = 300$. Together with the two data points for the global mean increases in $CH_4$ mixing ratios and isotope ratios, there are 302 observational data points. The summation over $j$, on the other hand, includes the isotopic composition ($^{13}CH_4$ content) of each source and the kinetic isotope effects of the $CH_4$ sinks, as well as two values representing the model initialization with a globally uniform $CH_4$ mixing ratio and a globally uniform $\delta^{13}CH_4$ isotope ratio.

The mathematical solution of this minimization problem is given by *Tarantola and Valette* [1982b] and *Tarantola* [1987] and also briefly mentioned by *Hein* [1994]. The information flow in the present inverse model is schematically summarized in Figure 4.

## 5. Atmospheric Observations

### 5.1. NOAA/CMDL Monitoring Network

Atmospheric $CH_4$ mixing ratios have been recorded regularly at the global cooperative air sampling network administered by the NOAA/CMDL. This network consists of approximately 30 stations covering latitudes from 82°N to 90°S. Since the network is primarily designed to be representative of unpolluted "background" air, many stations are located on remote islands, in the Arctic and in Antarctica. Several stations are also located on the Northern American continent, whereas large gaps exist on the other continents. Before 1990, there was not a single station on the Eurasian, African, and Southern American continents. A description of the sampling procedure and measurement methods is given by *Steele et al.* [1987], *Lang et al.* [1990a, b], and *Dlugokencky et al.* [1994a, b]. The data are available through the Carbon Dioxide Information Analysis Center in Oak Ridge, Tennessee [*Dlugokencky et al.*, 1994c].

In the present study, we selected the main target time period of 1983–1989, which is assumed to represent a quasi-stationary state of the global methane cycle. For sensitivity runs, performed to investigate apparent changes in the global atmospheric methane cycle since the 1980s, we selected the target time period 1991–1993. Unfortunately, not all stations of the NOAA/CMDL network were operating during a sizeable fraction of one or both of the target time periods. Hence only 25 stations for 1983–1989 and 21 stations for 1991–1993 were selected (Table 4).

Three more stations were excluded from the analysis because their particular local meteorological conditions were found to be not very well represented in the coarse-grid transport model: Cape Meares, Oregon (45°N), Key Biscayne, Florida (26°N), and Cape Grim, Tasmania (41°S). They are all lying either within or adjacent to a grid box with substantial $CH_4$ emissions. Therefore the model-calculated $CH_4$ mixing ratios are strongly influenced by these local emissions, whereas the reported observations are selected to reflect unpolluted, "background" air conditions. Thus a direct intercomparison of the modeled time averaged surface mixing ratio with the observations will inevitably be biased. It is difficult to correct for this bias without a detailed analysis of the applied data screening techniques in conjunction with a similar data selection procedure in the model (M. Ramonet and P. Monfray, $CO_2$ baseline concepts in 3-D atmospheric transport models, submitted to *Tellus*, 1996). Such an analysis, however, was not attempted in the present study.

The observations that enter the optimization procedure (equation (14)) were specified as monthly values and corresponding standard deviations of the $CH_4$ mixing ratio from each of the selected stations of the NOAA/CMDL network. These monthly values and standard deviation were determined from the individual flask measurements by means of a data analysis procedure which is similar to the standard analysis procedure employed by the carbon dioxide program of the Scripps Institution of Oceanography in La Jolla, California [*Keeling et al.*, 1989].

Specifically, we assumed that the observations at station $k$ can, for each target time period, be represented in the form

$$\chi_{\mathrm{obs},k}(t) = A_k + B(t - t_{\mathrm{mid}}) + S_{\mathrm{seas},k}(t) \qquad (15)$$

where $t_{\mathrm{mid}}$ denotes the midpoint of the selected target time period (i.e., mid-1986 or mid-1992, respectively), $A_k + B(t - t_{\mathrm{mid}})$ represents the linear trend, and $S_{\mathrm{seas},k}(t)$ represents the seasonal component consisting of the sum of the first four harmonic functions of the base period of 1 year. The constants $A_k$, $B$, and the coefficients of the harmonics of $S_{\mathrm{seas},k}(t)$ were determined from the individual flask measurements by the following procedure:

1. The sampling interval at each site of the NOAA/CMDL network is typically 1 week, with 2-3 reported flask measurements per sampling day. From all individual observations, we first computed daily aver-

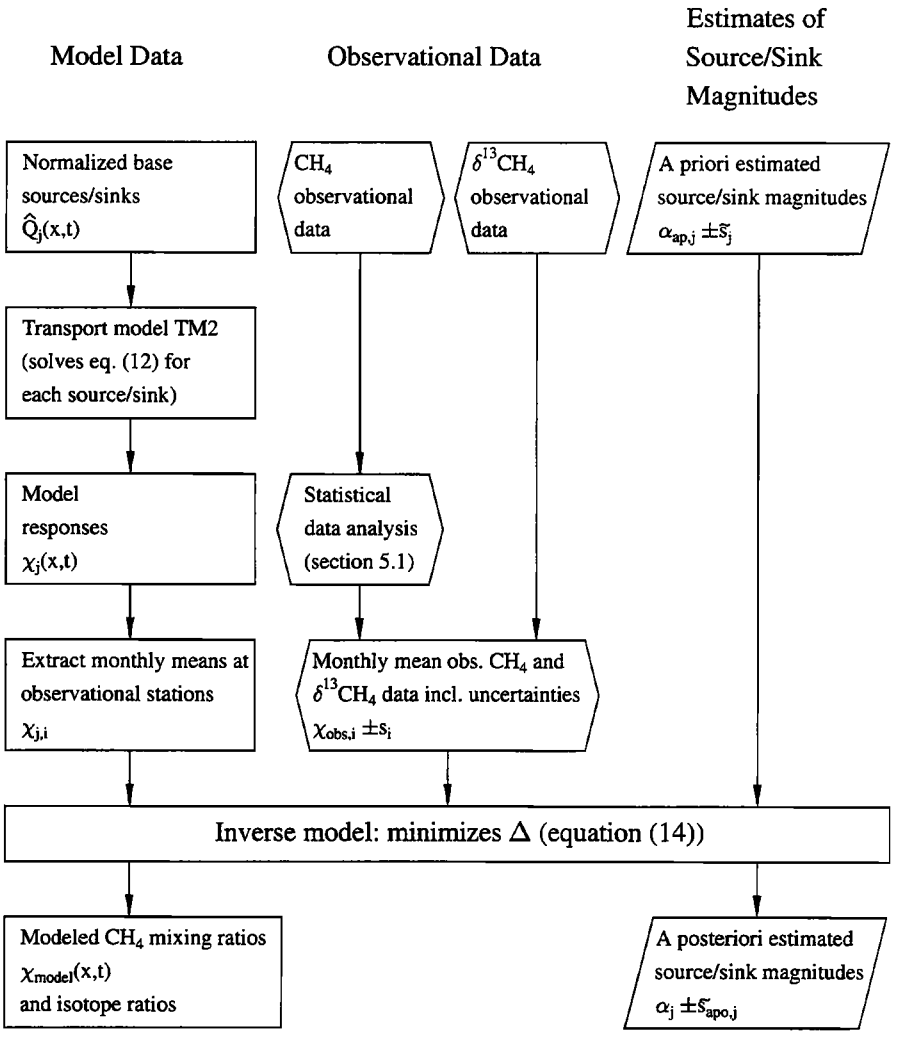


**Figure 4.** A schematic overview of the information flow in the present inverse model. There are three independent input data to the inverse model: (1) The contributions of the individual sources/sinks modeled with the transport model are based on prescribed geographical and temporal variability for each source/sink (sections 6.1 and 6.3). The geographical and temporal variablitity of the sink due to reaction with OH radicals is based on calculations with the coupled transport-chemistry model (section 2), (2) The atmospheric observations of $CH_4$ mixing ratios and $\delta^{13}CH_4$ isotope ratios are processed as explained in section 5.1, (3) A priori estimates of source/sink magnitudes are taken from literature (section 6.2). The a priori estimated magnitude of the sink due to reaction with OH is based on $CH_3CCl_3$ simulations (section 3). Also included are a priori estimates of the $^{13}CH_4$ content of the individual sources and kinetic isotope effects of the sinks (not displayed). The inverse model combines the input data and determines a posteriori estimates of source/sink magnitudes that minimize the weighted sum of squared deviations Δ (equation (14)). With these a posteriori estimates, it is also possible to calculate a global distribution of $CH_4$ mixing ratios (Figures 7 and 9) and isotope ratios (not shown) .

ages, thereby selecting only measurements flagged by NOAA/CMDL as representative of background air.

2. To the daily averages, we fitted a smooth function consisting of the sum of a stiff cubic spline trend and four harmonics. The latter are assumed to represent the seasonal cycle $S_{seas,k}(t)$ at the station $k$. The stiffness of the spline trend was controlled by specifying the time average of the squared second derivative. For all station records, this parameter was set to a value of 10 ppbv$^2$ yr$^{-4}$.

3. Subsequently, at each station, a linear function was fitted to the spline trend curves over the target time periods (i.e., over the time intervals 1983–1989 and 1991–1993). By evaluating this linear function at the centers of the target periods $t_{mid}$, the constant $A_k$ for the station $k$ was determined.

**Table 4.** NOAA/CMDL Methane Monitoring Sites Used in This Study

| Site Code | Latitude | Longitude | Altitude | Model Level | Site | Country | Mean $CH_4$ Mixing Ratio 1983–1989 | Mean $CH_4$ Mixing Ratio 1991–1993 |
|---|---|---|---|---|---|---|---|---|
| ALT | 82°N | 63°W | 210m | 1 | Alert, N.W.T. | Canada | 1740 | 1798 |
| MBC | 76°N | 119°W | 58m | 1 | Mould Bay, N.W.T. | Canada | 1742 | 1803 |
| BRW | 71°N | 157°W | 11m | 1 | Point Barrow, Alaska | U.S.A. | 1748 | 1805 |
| STM | 66°N | 2°E | 7m | 1 | Ocean Station "M" | Norway | 1735 | 1793 |
| CBA | 55°N | 163°W | 25m | 1 | Cold Bay, Alaska | U.S.A. | 1733 | 1791 |
| SHM | 53°N | 174°E | 40m | 1 | Shemya Islands, Alaska | U.S.A. | 1737 | 1794 |
| CMO | 45°N | 124°W | 30m | 1 | Cape Meares, Oregon | U.S.A. | 1720 | 1776 |
| NWR | 40°N | 106°W | 3475m | 4 | Niwot Ridge, Colorado | U.S.A. | 1693 | 1755 |
| AZR | 39°N | 27°W | 30m | 1 | Terceira Island, Azores | Portugal | 1712 | — |
| MID | 28°N | 177°W | 4m | 1 | Sand Island, Midway | U.S.A. | 1696 | 1756 |
| KEY | 26°N | 80°W | 3m | 1 | Key Biscayne, Florida Florida | U.S.A. | 1690 | 1748 |
| KUM | 20°N | 155°W | 3m | 1 | Cape Kumukahi, Hawaii | U.S.A. | 1678 | 1739 |
| MLO | 20°N | 156°W | 3397m | 4 | Mauna Loa, Hawaii | U.S.A. | 1661 | 1723 |
| AVI | 18°N | 65°W | 3m | 1 | St. Croix, Virgin Islands | U.S.A. | 1675 | — |
| GMI | 13°N | 145°E | 2m | 1 | Mariana Islands, Guam | U.S.A. | 1658 | 1722 |
| CHR | 2°N | 157°W | 3m | 1 | Christmas Island | Kiribati | 1629 | 1689 |
| SEY | 5°S | 55°E | 3m | 1 | Mahe Island | Seychelles | 1625 | 1684 |
| ASC | 8°S | 14°W | 54m | 1 | Ascension Island, Atlantic Ocean | England | 1613 | 1675 |
| SMO | 14°S | 171°W | 42m | 1 | Matatula Point, American Samoa | U.S.A. | 1608 | 1667 |
| AMS | 38°S | 78°E | 150m | 1 | Amsterdam Island, Indian Ocean | France | 1600 | — |
| CGO | 41°S | 145°E | 94m | 1 | Cape Grim, Tasmania | Australia | 1600 | 1662 |
| PSA | 65°S | 64°W | 10m | 1 | Palmer Station, Antarctica | U.S.A. | 1598 | 1663 |
| SYO | 69°S | 40°E | 11m | 1 | Syowa, Antarctica | Japan | 1599 | 1663 |
| HBA | 75°S | 27°W | 10m | 1 | Halley Bay, Antarctica | England | 1597 | — |
| SPO | 90°S | — | 2810m | 1 | Amundsen Scott (South Pole) | U.S.A. | 1598 | 1662 |

4. The quasi-stationarity assumption implies a globally uniform annual increase in the $CH_4$ mixing ratio. This globally averaged time trend $B$ was determined by averaging the time trends as determined in step 3 for each station. During 1983–1989, we obtained an annual increase of $11.9 \pm 0.3$ ppbv, and during 1991–1993, the increase was calculated to be $6.9 \pm 2$ ppbv. The uncertainties in these numbers were chosen according to *Dlugokencky et al.* [1994b] and *Steele et al.* [1992]. Here and throughout this study, uncertainty figures represent double standard deviations ($2\sigma$) if not stated otherwise.

5. For each target time period, the monthly mean values $\chi_{obs,i}$ to be used in the inverse model were then calculated by evaluating equation (15) for each month of the central year of the appropriate target time interval (i.e., for 1986 and 1992, respectively).

6. Finally, the standard deviation $s_i$ of each monthly mean value was taken to be the root mean squared residual between daily averages and fitted trend curve.

### 5.2. Atmospheric $^{13}CH_4/^{12}CH_4$ Isotope Ratio Observations

Monthly means and standard deviations of the $^{13}C/^{12}C$ ratio of atmospheric $CH_4$ were taken from *Quay et al.* [1991] for Point Barrow, Alaska (71°N), Olympic Peninsula, U.S. west coast (48°N), and Mauna

**Table 5. Characterization of Atmospheric Methane Sources and Sinks**

| Source/Sink | Spatial Variation | Temporal Variation | Reference |
|---|---|---|---|
| Domestic animals | depending on animal population | none | *Lerner et al.* [1988] and *Crutzen et al.* [1986] |
| Rice paddies | predominantly in Southeastern Asia | depending on growing season | *Aselmann and Crutzen* [1989] |
| Bogs | predominantly north of 50°N | depending on temperature ($Q_{10} = 1.5$) | *Matthews and Fung* [1987] |
| Swamps | predominantly in tropical regions | none | *Matthews and Fung* [1987] |
| Waste treatment | according to statistics on biodegradeable carbon dumped in landfills | none | *Bingemer and Crutzen* [1987] |
| Biomass burning | predominantly between 25°N and 25°S | in dry season | *Hao et al.* [1990] |
| Coal, oil, and gas | see reference | none | *Selzer and Zittel* [1990] |
| Reaction with OH | maximum in tropics | maximum in spring-summer | this work |
| Stratospheric loss | maximum in tropics | | *Brühl and Crutzen* [1993] and C. Brühl (personal communication, 1993) |
| Uptake by soils | land surfaces, reduced in deserts | under frost-free conditions only | *Dörr et al.* [1993] |

Loa, Hawaii (20°N). Unfortunately, $^{13}C/^{12}C$ ratios in atmospheric $CH_4$ from the southern hemisphere are only available from one single station (Baring Head, New Zealand, 41°S [*Lassey et al.*, 1993]). Since these measurements first started in August 1989, near the end of our base target time period, they were not included in the present inverse model calculations.

Neither the data reported by *Quay et al.* [1991] nor that of *Lassey et al.* [1993] show an annual trend significantly different from zero. On the basis of this, we chose a globally averaged annual time trend of the $^{13}C/^{12}C$ ratio of $0 \pm 0.06‰$.

### 5.3. The global $^{14}CH_4$ budget

Because the only known $^{14}C$-free methane sources are those related to fossil fuels and all other important methane sources have a nearly identical $^{14}C$ content, the total of all fossil fuel related methane sources can be calculated from global $^{14}CH_4$ budget calculations. Recent estimates of the fraction of fossil fuel related $CH_4$ emissions are $21 \pm 3\%$ [*Wahlen et al.*, 1989], $21 \pm 4\%$ [*Manning et al.*, 1990], and $16 \pm 12\%$ [*Quay et al.*, 1991]. The relatively high uncertainty given by *Quay et al.* [1991] is mainly caused by significant (and poorly known) $^{14}CH_4$ releases from the nuclear industy, e.g. pressurized water reactors [*Kunz*, 1985]. These fractions correspond to fossil fuel related $CH_4$ sources of $100 \pm 18$ Tg/yr [*Crutzen*, 1995]. In two scenario calculations with alternative a priori source magnitude estimates, a numerical value of $100 \pm 25$ Tg/yr [*Prather et al.*, 1995] was applied.

## 6. Base Methane Source and Sink Components

### 6.1. Geographical and Temporal Variation of Sources

The base source and sink components which were considered in the present study are listed in Table 5. The geographical and temporal variation of many source components in this study are based on data sets identical or similar to those used by *Fung et al.* [1991]. In particular, we consider the methane sources from the following:

**6.1.1. Domestic animals.** The spatial distribution of domestic animals was taken from animal population statistics [*Lerner et al.*, 1988]. The methane emissions from different animal types were weighted according to the values given by *Crutzen et al.* [1986]. No seasonal variation was assumed.

**6.1.2. Rice paddies.** Cultivated rice paddy areas for each calendar month were taken from *Aselmann and Crutzen* [1989], who based their compilation on a country-by-country assessment of rice paddies by J. Richards in the work by *Darmstädter et al.*, 1987 (cited from *Aselmann and Crutzen* [1989]). Their estimated global rice harvest area totals $1.3 \times 10^6$ km$^2$, of which nearly 90% is located in Asia. *Aselmann and Crutzen* [1989, p. 335] claim that "a cultivation cycle (typically) lasts for 4 to 5 months in most countries and is restricted to the rainy season ... Year-round cultivation is only found in some Asian countries in the humid tropics with no pronounced wet and dry season such as Indone-

sia, the Phillipines, or Taiwan." Lacking more detailed information about the temporal variation of $CH_4$ emissions from rice paddies, we assume constant $CH_4$ fluxes per area throughout the cultivation period.

**6.1.3. Natural wetlands.** The geographical distribution of natural wetland areas was taken from the data compilation of *Matthews and Fung* [1987]. In our definition, swamps correspond to the three categories of nonforested and forested swamps as well as alluvial formations in Matthews' and Fung's database, and bogs simply combine their two categories of nonforested and forested bogs. $CH_4$ emissions from wetlands strongly depend on several factors including temperature, water table, and biological conditions. These conditions show a high diversity between different locations. It is beyond the scope of this study to develop a detailed model of $CH_4$ emissions from wetlands. Therefore, we simply assumed no temporal variation in methane emission rates from swamps, which are mainly located in the tropics. Bogs, on the other hand, are predominantly located north of 50°N, where the prevailing seasonal temperature variations are much more pronounced than in tropical regions. In this study, we assumed a simple dependence of $CH_4$ emission fluxes $F$ from bogs on the monthly mean surface air temperature $T$,

$$F = F_0 Q_{10}^{(T-T_0)/10K}, \qquad (16)$$

with a $Q_{10}$ factor of 1.5. Higher $Q_{10}$ factors (in particular $Q_{10} = 2$, as assumed by *Fung et al.* [1991]) lead to unrealistic seasonal variations of $CH_4$ mixing ratios at high northern latitudes in the model. Nevertheless, it is important to note that other assumptions regarding the time dependence of $CH_4$ emissions from wetlands could also be justified and would alter the results of the inverse model. The development of an improved parametrization of $CH_4$ emissions from wetlands based on direct emission flux measurements would be highly desirable.

**6.1.4. Landfills.** $CH_4$ emissions from landfills were assumed to be proportional to the amount of biodegradeable organic carbon (DOC) dumped. *Bingemer and Crutzen* [1987] estimated that approximately 75% of the DOC in landfills originate from municipal solid wastes (MSW), and 25% come from industrial wastes. We assumed the geographical distribution of industrial wastes to be identical to the distribution of $CO_2$ emissions from fossil fuel combustion taken from the compilation of *Marland et al.* [1985]. The geographical distribution of DOC from MSW was based on per capita estimates made for four regions (135 kg/yr in the U.S.A., Canada, and Australia, 40 kg/yr in other Organization for Economic Cooperation and Development (OECD) countries, 32 kg/yr in the former Soviet Union and Eastern Europe, and 22 kg/yr in urban regions in other parts of the world). For each horizontal model grid box, these per capita estimates were multiplied with the human population in this grid box, derived from the human population density map for 1984 compiled by *Fung et al.* [1991]. It was assumed that $CH_4$ emissions from landfills do not show any seasonal variation.

**6.1.5. Biomass burning.** For methane emissions from biomass burning, we used the data compilation by *Hao et al.* [1990], who mapped the total amount of biomass burned each year in tropical Africa, America, and Asia. The temporal distribution of biomass burning given by *Hao et al.* [1990] is based on climatological precipitation statistics [*Jaeger*, 1976] from which the timing of the dry period was derived. However, this temporal distribution of biomass burning is relatively uncertain. Improved maps of global biomass burning based on satellite observations will hopefully be available in the near future.

**6.1.6. Fossil fuel related emissions.** The geographical distribution of methane emissions related to fossil fuel production was taken from *Selzer and Zittel* [1990], who estimated these emissions from the oil, gas, and coal industry on a regional basis. These estimates take into account various loss processes during exploitation, transport, processing, and burning of fossil fuels. Nevertheless, the high variablity of the $CH_4$ emission factors assigned to these processes involves large uncertainties. For instance, $CH_4$ release from coal strongly differs from one mine to another (and even within one mine) depending, for example, on age and depth of the extracted coal. $CH_4$ emissions from the oil and gas industry are generally believed to be less certain than those from the coal industry. Therefore, a scaling of fossil fuel related $CH_4$ emissions to production figures leads to high uncertainties. Unfortunately, reliable data on $CH_4$ emissions from the coal, gas, and oil industries are presently not available. Since there are no indications of strong seasonal variations in the fossil fuel related $CH_4$ emissions, they were assumed to be constant throughout the year. Because the emissions from the Siberian gas industry are highly uncertain and subject to much speculation, this source was treated separately in this study. This Siberian gas source was assumed to be located east of, but close to, the Ural mountains, where the most important Russian gas fields are found. Emissions were assumed to occur in the two TM2 model grid boxes located between 54.8°N and 70.4°N and between 65°E and 75°E.

**6.1.7. Other sources.** Other potential sources of atmospheric methane have been suggested in the literature, in particular termites, hydrate destabilization, and methane release from shallow lakes, ocean shelves, and estuaries. All these sources are either speculative or their geographical distribution, which is critical for the present inverse modeling approach, is poorly known.

Since it is very unlikely that the total of these sources exceeds 10% of all atmospheric methane sources, they have been neglected in the present study.

### 6.2. A Priori Estimates of Source Magnitudes and Their Uncertainties

In principle, the present inverse modeling approach requires that a priori estimates of source magnitudes and their uncertainties be prescribed independently from the atmospheric observations. In reality, this is difficult to achieve, since all estimates of $CH_4$ source magnitudes published in the literature already explicitly or implicitly use information based on atmospheric $CH_4$ observations. Nevertheless, we ignore this interdependence of a priori source magnitude estimates and atmospheric $CH_4$ observations. This has implications that are discussed in section 7.2.3.

Estimates of source magnitudes and assessments of their uncertainties vary significantly between different authors. In order to investigate how the choice of these a priori estimates influences the results of the inversion, two different sets of a priori estimates, one based on *Crutzen* [1995] and the other one on the Intergovernmental Panel on Climate Change (IPCC) 1994 scientific assessment [*Prather et al.*, 1995] were used. In addition, the a priori uncertainties assigned to these estimates were varied.

For mathematical convenience, we always assumed the source magnitudes to have a Gaussian probability density centered around the stated best estimates. Despite the fact that the published ranges do not always provide a strong statistical analysis of uncertainties of the various methane source magnitudes, we interpreted the stated ranges as 95% confidence intervals (or double standard deviations).

### 6.3. Sinks

The main sink of atmospheric methane is its oxidation initialized by reaction with OH radicals. The global distribution of OH radicals in the troposphere was calculated with the three-dimensional global atmospheric transport-chemistry model as described in section 2. The a priori estimated global magnitude of the OH sink applied in the inverse model has been determined by modeling the atmospheric concentration of $CH_3CCl_3$, presented in section 3 of this work. Its uncertainty was estimated to be $\pm$ 20%, mainly due to the uncertainties of the rate coefficients for the reactions of OH with $CH_3CCl_3$ and $CH_4$. It is important to note that the temporal and geographical variability of OH concentrations calculated with the chemical model is sustained by the application of the global uniform correction factor determined from modeling $CH_3CCl_3$. Any significant error in this variability would, of course, lead to incorrect estimates of $CH_4$ source magnitudes. Despite the fact that there are no indications that the calculated OH distribution is unrealistic (sections 2.3 and 3), the reliability of the calculated OH concentrations cannot exactly by quantified.

Another significant $CH_4$ sink is its destruction in the stratosphere by photolysis and reactions with OH, Cl, and $O(^1D)$. The two-dimensional photochemical model developed at the Max-Planck-Institut für Chemie [*Brühl and Crutzen*, 1993] was employed to calculate the amount of $CH_4$ destroyed in the stratosphere in each calendar month, latitude belt, and vertical model level. In each of the two stratospheric TM2 model levels, the sum of the destruction rates of the appropriate levels of the two-dimensional photochemical model was applied.

Microbiological destruction of $CH_4$ occurring in areated soils also plays an important role in the global methane budget. In this study, the global map of $CH_4$ uptake by soils compiled by *Dörr et al.* [1993] was adopted.

Tropospheric reaction with atomic chlorine (Cl) is a minor $CH_4$ sink, probably not contributing to more than 1 or 2% of all $CH_4$ sinks. Because of its high isotopic fractionation factor [*Saueressig et al.*, 1995], however, it might have a small effect on the distribution of $\delta^{13}CH_4$ isotope ratios in the troposphere, if Cl concentrations in the marine boundary layer are at the higher end of ranges proposed by different authors [*Pszenny et al.*, 1993; *Singh et al.*, 1996; *Wingenter et al.*, 1996]. In this study, a possible contribution of Cl atoms acting as additional tropospheric $CH_4$ sink is neglected.

### 6.4. $^{13}CH_4$ Content of Sources and Kinetic Isotope Effects

A priori estimates of the $^{13}CH_4$ content of the different sources and their uncertainties were taken from *Levin* [1994]. The mean $\delta^{13}C$ signature of global $CH_4$ sources must be lower than the mean atmospheric $\delta^{13}CH_4$ value, since all known $CH_4$ sinks remove $^{12}CH_4$ faster from the atmosphere than $^{13}CH_4$. A quantitative assessment of the kinetic isotope effects (KIEs) is therefore important if we want to use atmospheric $\delta^{13}CH_4$ observations to constrain methane source magnitudes. The most recently measured deviation of the rate coefficient for the reaction of OH with $^{13}CH_4$ relative to the reaction with $^{12}CH_4$ is $k_{13}/k_{12} - 1 = -5.4 \pm 0.9‰$ [*Cantrell et al.*, 1990], corresponding to a much lower KIE than earlier estimates. For uptake of $CH_4$ in areated soils, *King et al.* [1989] measured a fractionation constant ($k_{13}/k_{12} - 1$) of $-21 \pm 10‰$. Recent atmospheric $^{13}CH_4/^{12}CH_4$ isotope ratio measurements in the lower stratosphere made by *Brenninkmeijer et al.* [1995] showed a strong increase in $\delta^{13}CH_4$ values with decreasing $CH_4$ mixing ratios. They attributed this to the fact that, in the stratosphere, some $CH_4$ reacts with Cl. According to recent laboratory mea-

surements, this reaction with Cl shows an enormous fractionation ($k_{13}/k_{12} - 1 = -66 \pm 2‰$ at 297 K), much larger than the reaction of $CH_4$ with OH [*Saueressig et al.*, 1995]. In agreement with the measurements of *Brenninkmeijer et al.* [1995], we apply an overall KIE for stratospheric $CH_4$ destruction corresponding to $k_{13}/k_{12} - 1 = -12 \pm 4‰$.

## 7. Results and Discussion

In this section, the results of the inverse model calculations are presented and discussed. The various scenario calculations are labeled $S_0, S_1, \ldots, S_8$. Their main characteristics are summarized in Table 6. The second column indicates whether the base source and sink components have been modified compared to the base scenario $S_1$. In scenario $S_0$, they have been chosen as explained in sections 6.1 and 6.3. In scenario $S_1$, the time dependence of the emissions from bogs has been modified (section 7.1.1). In scenario $S_3$, the transport model TM2 was driven with ECMWF's meteorological analyses for the year 1986, whereas all other scenarios are based on the meteorological analyses for 1987. In the third column of Table 6, the references for the a priori estimates of the source magnitudes are given. Column four indicates whether sources and sinks are adapted by the inverse model (scenarios $S_0 - S_8$), or only source magnitudes are optimized and sink magnitudes are held constant at their a priori estimates (scenarios $S_7$ and $S_8$). The measurements used to constrain methane source and sink magnitudes in the corresponding scenario are given in column five. In all scenarios, the atmospheric observations of $CH_4$ mixing ratios from the NOAA/CMDL Cooperative Flask Sampling Network have been used as discussed in section 5.1 (indicated by "$CH_4$"). In scenarios $S_4$ and $S_5$, only the $CH_4$ data from those stations that were operational during a sizeable fraction of both target time periods (1983–1989 and 1991–1993) were used. In all other scenarios, the four stations that measured $CH_4$ during the 1983–1989 target time period, but not in 1991–1993, were also included. In all scenarios, the global mean increase in the atmospheric $CH_4$ mixing ratios during the appropriate target time periods has been used as an additional constraint for the global $CH_4$ budget. In all scenarios except $S_2$, the $\delta^{13}CH_4$ observations [*Quay et al.*, 1991] have also been used (indicated by "$\delta^{13}CH_4$"). The last column specifies the target time period selected for the appropriate scenario.

For each scenario, the optimized (a posteriori) estimates of source and sink magnitudes are given in Tables 7, 9, or 10. The second column of each of these tables gives the a priori estimates belonging to each scenario included in the corresponding table. No a priori estimate has been made for the individual contributions of bogs and swamps to the total wetland source or for the Siberian gas and the oil/other gas source to the total fossil fuel related sources. Technically, this was achieved by setting the uncertainties of the appropriate a priori estimates to the very high value of 1000 Tg/yr. The values given in parentheses are only applied for forward model calculations with the a priori estimated emission magnitudes, which are displayed in Figures 5, 6, 10, and 11.

The a posteriori estimates of $CH_4$ emissions from bogs and swamps are, however, restricted by the estimated total wetland emissions. The subdivision of the total wetland emissions among bogs and swamps is solely derived from the inverse model that connects the geographical and temporal distribution of bogs and swamps with atmospheric $CH_4$ measurements. The subdivision of the fossil fuel related sources is deter-

**Table 6.** Brief Characterization of Scenarios Used in This Work

| Scenario | Base Source Components [a] | Basis of a Priori Source Magnitude Estimates | Optimization of Sources and Sinks (S and S) or Sources Only (S) | Applied Atmospheric Measurements | Target Time Period |
|---|---|---|---|---|---|
| $S_0$ | T dependence of bogs (see text) | *Crutzen* [1995] | S and S | $CH_4$, $\delta^{13}CH_4$ | 1983–1989 |
| $S_1$ | — | *Crutzen* [1995] | S and S | $CH_4$, $\delta^{13}CH_4$ | 1983–1989 |
| $S_2$ | — | *Crutzen* [1995] | S and S | $CH_4$ only | 1983–1989 |
| $S_3$ | 1986 winds | *Crutzen* [1995] | S and S | $CH_4$, $\delta^{13}CH_4$ | 1983–1989 |
| $S_4$ | — | *Crutzen* [1995] | S and S | $CH_4$, [b] $\delta^{13}CH_4$ | 1983–1989 |
| $S_5$ | — | *Crutzen* [1995] | S and S | $CH_4$, [b] $\delta^{13}CH_4$ | 1991–1993 |
| $S_6$ | — | *Prather et al.* [1995] | S and S | $CH_4$, $\delta^{13}CH_4$ | 1983–1989 |
| $S_7$ | — | *Crutzen* [1995] | S | $CH_4$, $\delta^{13}CH_4$ | 1983–1989 |
| $S_8$ | — | *Prather et al.* [1995] | S | $CH_4$, $\delta^{13}CH_4$ | 1983–1989 |

[a] Only differences to $S_1$ are indicated.
[b] restricted to those stations that were operational during a sizeable fraction of both target time periods.

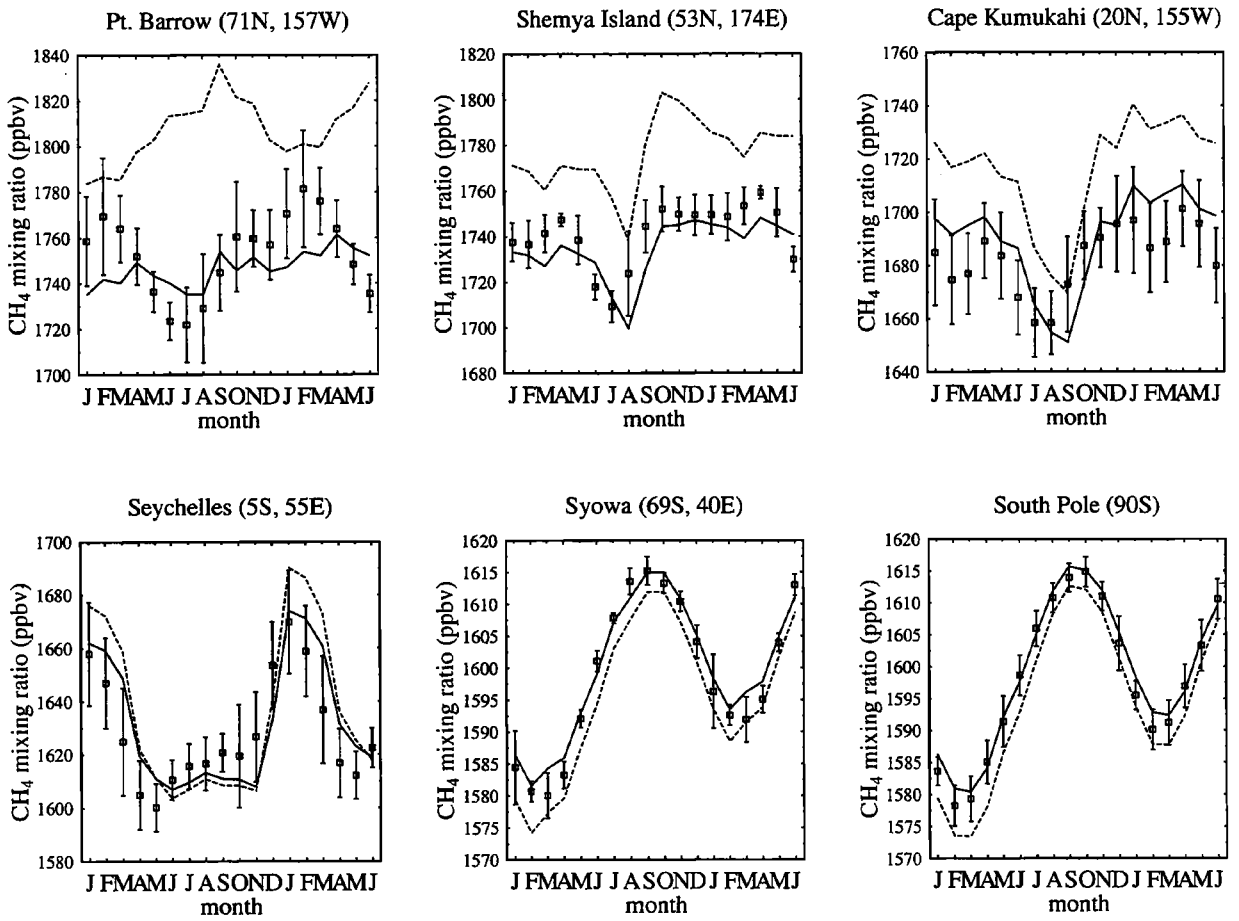


**Figure 5.** Simulated (dotted line, a priori scenario; solid line, scenario $S_0$) and observed (squares with $1\sigma$ error bars) $CH_4$ mixing ratio at selected NOAA/CMDL stations [*Dlugokencky et al.*, 1994c]. The months of January to June are displayed twice in order to reveal the seasonal cycle more clearly.

mined similarly. Additionally, the $CH_4$ emissions from the coal industry are separately constrained by an a priori estimate.

### 7.1. Base Scenarios

**7.1.1. Preliminary base scenario ($S_0$).** The a posteriori estimates of source magnitudes and their uncertainties resulting from the inversion procedure, together with a priori estimates as described above, are shown in Table 7 in the column labelled $S_0$. Figure 5 shows the modeled $CH_4$ mixing ratios using both the a priori and the a posteriori emission estimates in comparison with the observations made at the NOAA/CMDL stations. The sites shown here were selected to represent different latitudes. It can be seen that the agreement between the a posteriori modeled $CH_4$ mixing ratios and the observations is very good except for high northern latitudes, where the seasonal cycle is not well simulated. This discrepancy at high northern latitudes may possibly be attributed to an incorrect description of the temporal variations of $CH_4$ emissions from bogs, the source with the most pronounced seasonal variability at these latitudes. Despite the fact that we did not develop a comprehensive and detailed model of $CH_4$ emissions from wetlands, we tried to obtain an improved agreement of model results with the observed methane mixing ratios at high northern latitudes by introducing simple modifications in the time dependence of $CH_4$ emissions from bogs. Indeed, the assumption that $CH_4$ emissions from bogs respond to surface air temperature changes with a time delay of 2 months improved the situation substantially. This time lag might also be justified by the fact that $CH_4$ emissions from bogs follow are not directly determined by air temperature but by soil temperature which usually lags air temperature by several weeks. We therefore used this modified characterization of $CH_4$ emissions from bogs in the modified base scenario ($S_1$) and all subsequent model calculations. It is, however, important to note that the model resolution is insufficient to adequately describe the planetary

**Table 7.** A Priori and a Posteriori Methane Source and Sink Magnitude Estimates for the Time Period 1983–1989

| Source/ Sink | A Priori [*Crutzen*, 1995] | A Posteriori $S_0$ (Preliminary Base Scenario) | $S_1$ (Modified Base Scenario) | $S_2$ (No $^{13}C$) | $S_3$ (1986 Winds) | $S_7$ (Sinks Fixed) |
|---|---|---|---|---|---|---|
| Animals[a] | 110±22 | 92±20 | 90±20 | 90±21 | 84±20 | 89±20 |
| Rice | 80±60 | 83±23 | 69±23 | 78±26 | 75±24 | 74±20 |
| Wetlands | 270±50 | 231±27 | 232±27 | 228±28 | 239±27 | 235±19 |
| Bogs | (100)[b] | 35±8 | 44±8 | 35±14 | 49±9 | 44±8 |
| Swamps | (170)[b] | 196±26 | 188±25 | 192±26 | 190±26 | 191±17 |
| Landfills | 40±20 | 43±15 | 40±15 | 41±15 | 36±15 | 40±15 |
| Biomass burning | 40±20 | 43±11 | 41±11 | 41±11 | 27±11 | 42±11 |
| Fossil sources | 100±18 | 100±15 | 103±15 | 102±16 | 101±15 | 103±15 |
| Coal | 35±10 | 32±10 | 33±10 | 32±10 | 34±10 | 33±10 |
| Siberian gas | (20)[b] | 36±13 | 34±13 | 43±18 | 25±13 | 33±13 |
| Oil and other gas | (45)[b,c] | 32±23 | 36±23 | 27±25 | 41±22 | 37±22 |
| Tropospheric OH | -480±96[d] (-530)[b] | -488±30 | -469±30 | -474±31 | -452±29 | -480[e] |
| Stratosphere | -40±8 | -45±8 | -44±8 | -45±8 | -46±8 | -40[e] |
| Soil uptake | -30±15 | -26±14 | -28±14 | -28±14 | -31±14 | -30[e] |
| Atmospheric increase | 33.4±0.8 | 33.6±0.8 | 33.6±0.8 | 33.6±0.8 | 33.6±0.8 | 33.6±0.8 |
| Total emissions | 640 | 592 | 575 | 580 | 562 | 584 |
| $X^2$ ($CH_4$ data only) | 8.51 | 1.01 | 0.90 | 0.89 | 1.03 | 0.91 |
| $X^2$ ($CH_4$ and $\delta^{13}CH_4$ data) | 8.42 | 1.07 | 0.89 | | 0.98 | 0.90 |

Uncertainties represent 95% confidence intervals ($2\sigma$); units are in Teragrams per year except for $X^2$, which is expressed in terms of $\sigma^2$.

[a] including animal wastes.

[b] Values in parentheses were not used for inverse modeling but only applied in forward model calculations (see text).

[c] by difference (total fossil minus other fossil sources).

[d] calculated with the three-dimensional transport-chemistry model TM2 in this study.

[e] Fixed sink magnitudes.

boundary layer (PBL). Especially at high latitudes in winter, with prevailing low inversion heights, the model may overestimate vertical mixing between the PBL and the free troposphere. This deficiency could be responsible for the underestimation of the seasonal variation of $CH_4$ mixing ratios at high northern latitudes.

**7.1.2. Modified base scenario ($S_1$).** The modeled $CH_4$ mixing ratios for the complete set of the NOAA/CMDL stations used in this study, both for the a priori and the a posteriori emission estimates, are shown in Figure 6 together with results from a sensitivity run which will be described later. Compared to scenario $S_0$ (Figure 5), the calculated seasonality at high northern latitudes has improved significantly, although the seasonal amplitude is still underestimated in the model. At all other stations, differences between both scenarios are small.

In Table 7 the column labelled $S_1$ (modified base scenario) contains the a posteriori estimates of $CH_4$ sources and sinks. The major changes in source estimates are somewhat lower emissions from animals, rice and wetlands, whereas the estimated source magnitudes for landfills, biomass burning and fossil sources are nearly identical to their a priori estimates. Nevertheless, all a posteriori source estimates are within the ranges given by the a priori uncertainties. It can thus be concluded that the a priori source estimates by *Crutzen* [1995] are, within the stated uncertainties, consistent with the atmospheric $CH_4$ observations. Since the a priori estimated emissions lead to a slightly overestimated north-south gradient in atmospheric $CH_4$ mixing ratios, reduced emissions from animals, rice, and bogs, which are all mainly located in the northern hemisphere, yield a better agreement to the observations.

The modeled annual and zonal mean $CH_4$ mixing ratios are shown in Figure 7. It clearly shows the north-south gradient of approximately 140 ppbv which results from the fact that most sources are located in the northern hemisphere (see also Figure 8). Furthermore, within the northern hemisphere, there is a north-south gradient because at high northern latitudes, sources exceed sinks, resulting in a flux of $CH_4$ toward the equa-

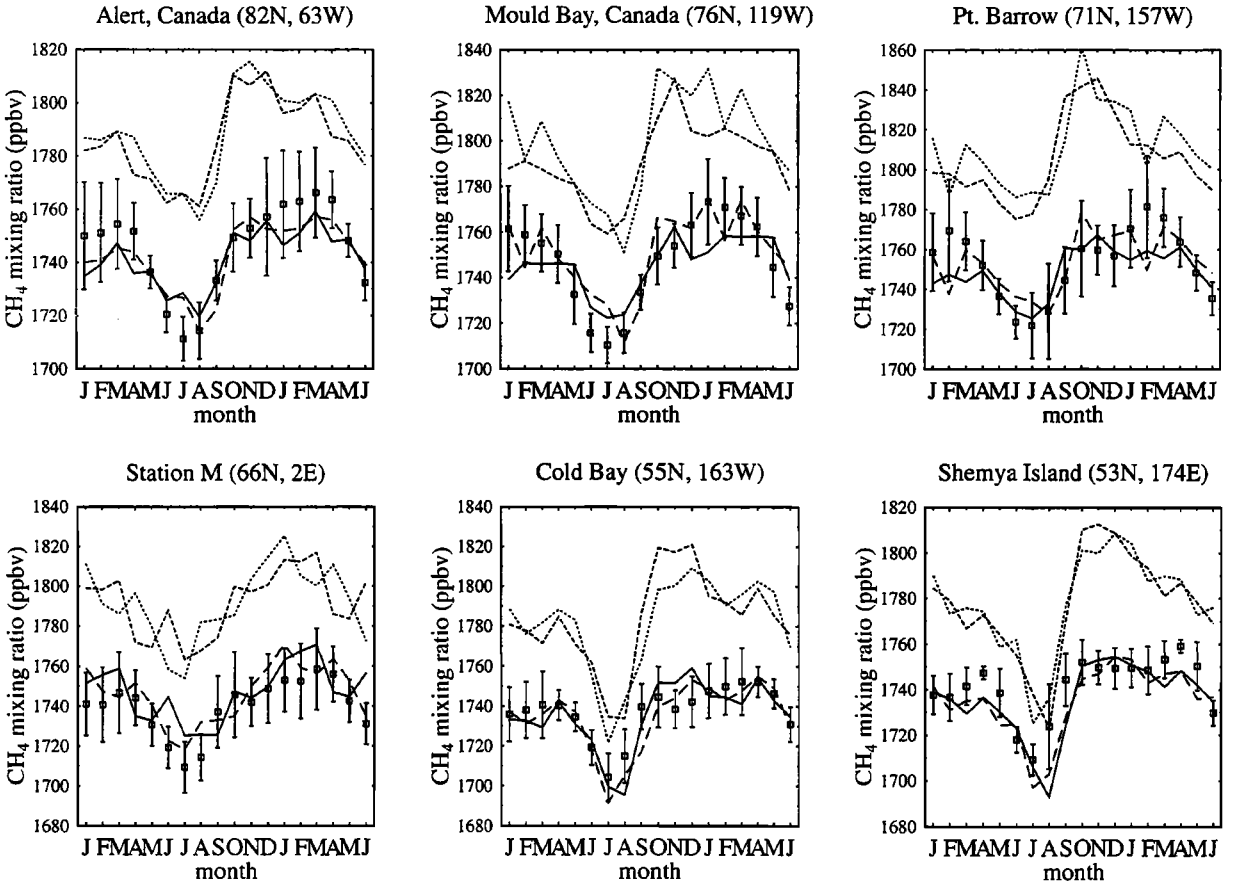


**Figure 6.** Simulated (dotted and solid lines, a priori scenario and scenario $S_1$ using 1987 wind data; short-dashed and long-dashed line, a priori scenario and scenario $S_3$ using 1986 wind data in the transport model) and observed (squares with $1\sigma$ error bars) $CH_4$ mixing ratio at selected NOAA/CMDL stations [*Dlugokencky et al.*, 1994c]. The months of January to June are displayed twice in order to reveal the seasonal cycle more clearly.

tor. In the southern hemisphere, on the other hand, the southward $CH_4$ flux is driven by the inflow of $CH_4$ from the northern hemisphere and the absence of substantial sources at middle or higher latitudes (Figure 8).

In Figure 9, showing the annual mean methane mixing ratios near the surface, the north-south gradient can again be seen, and the maxima over all continents except Antarctica are also apparent. According to the model simulations, the worldwide highest mixing ratios occur over central Europe and the former Soviet Union, where fossil fuel related sources (e.g., Siberian gas), bogs, domestic animals, and waste treatment are the most important methane sources. The high values seen over China and India can be attributed to emissions from rice paddies and the high cattle population in India. For the maximum in the eastern United States and Canada, cattle, wetlands, fossil fuel related sources, and landfills are responsible. The central African and southern American maxima are predominantly due to biomass burning and swamps; in southern America, cattle are also important.

The fact that the model can adequately reproduce phase and amplitude of the seasonal variation at the Antarctic stations (Figure 6), far away from methane sources, confirms that the seasonal variation of modeled OH concentrations in the southern hemisphere should be quite realistic. However, it is important to note that seasonal variations in methane at the Antarctic stations are also influenced by transport from the northern hemisphere and from tropical southern hemispheric sources, especially biomass burning. Both interhemispheric transport and tropical sources have a strong seasonality that shows a significant interannual variability which was not taken into account in the model because the meteorological data applied in the model was always taken from ECMWF's analyses of the year 1987.

The mean annual meridional profile of $CH_4$ mixing ratios (Figure 10a) confirms that the north-south gradient can be very well simulated in the model. This statement is also true for the $^{13}C/^{12}C$ isotope ratios (Figure 10b), at least as far as atmospheric $^{13}CH_4/^{12}CH_4$ measurements existed for the 1980s.

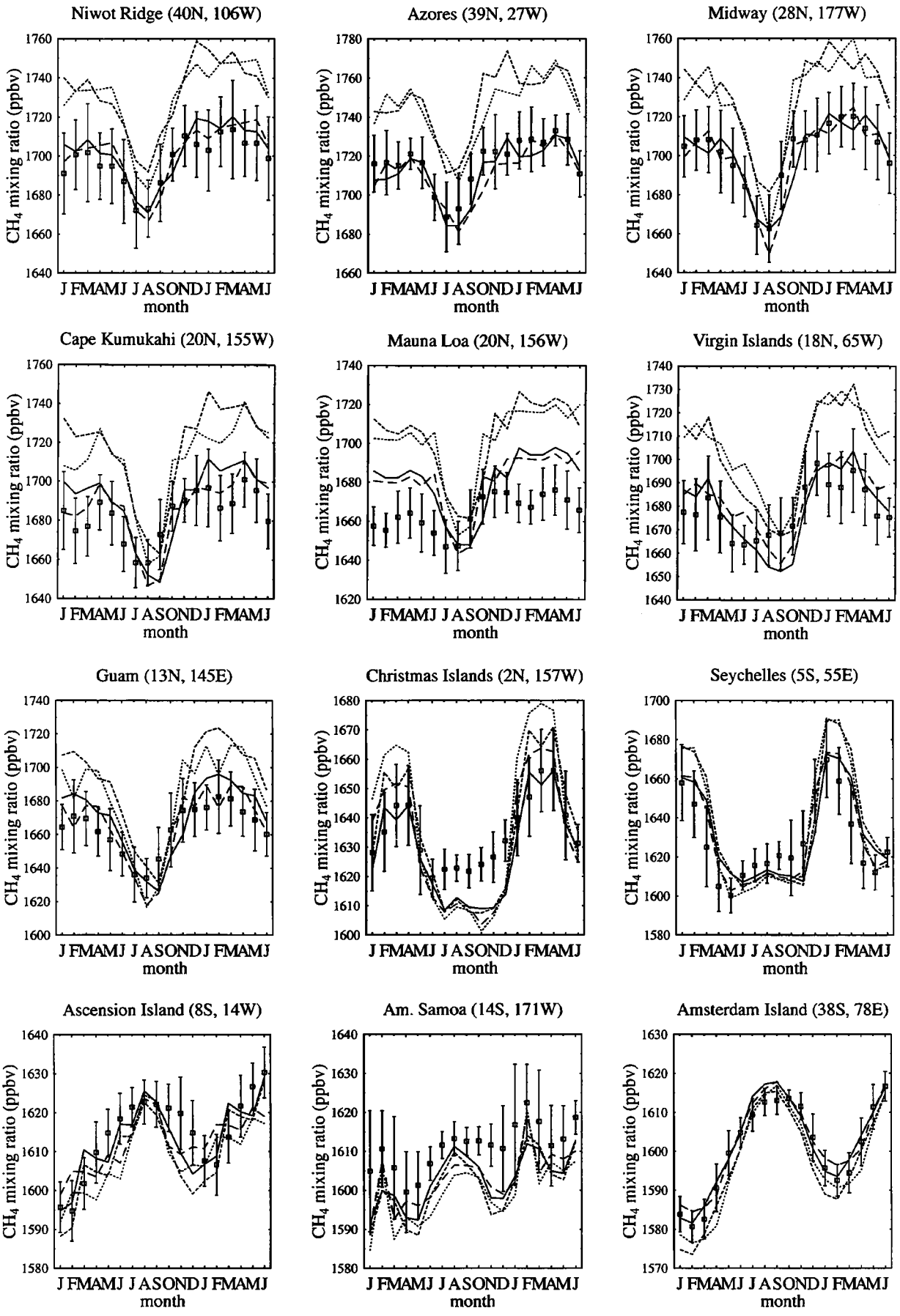


**Figure 6. (continued)**

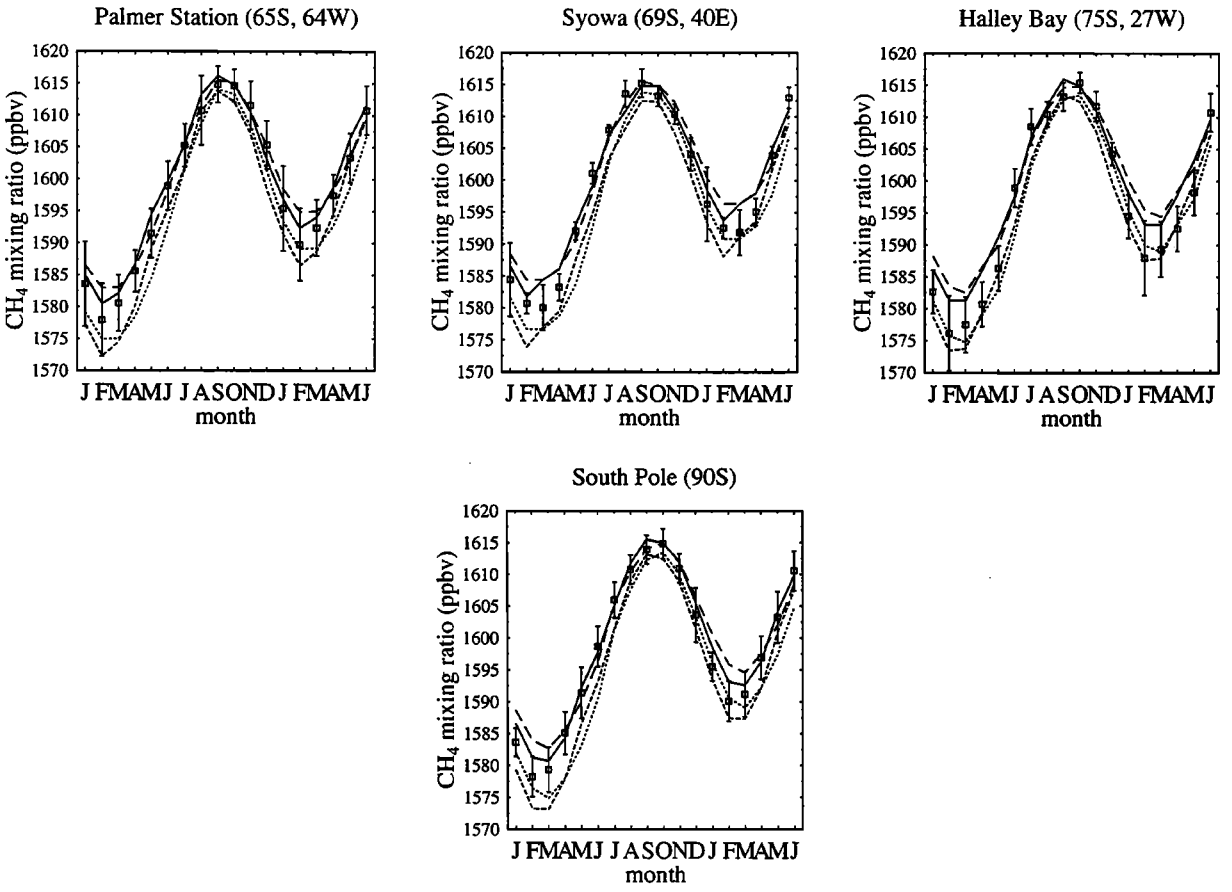


**Figure 6.** (continued)

Modeled seasonal variations in $^{13}C/^{12}C$ isotope ratios in atmospheric methane are generally in phase with the observations (Figure 11). Their amplitude is overestimated in the a priori scenario but well simulated with the a posteriori estimates of emissions and adopted $^{13}C$ content of sources and KIE's (Table 8). Although this is very promising, more $\delta^{13}CH_4$ measurements are necessary to make a more sound comparison.

### 7.2. Sensitivity Studies

**7.2.1. Information content of $^{13}C/^{12}C$ observations (scenario $S_2$).** To investigate the information content of isotope observations, we run the inverse model ignoring the atmospheric $^{13}CH_4$ observations and compare the resulting a posteriori emission estimates and their uncertainties (scenario $S_2$) with the standard scenario ($S_1$). With two exceptions, the a posteriori uncertainties in scenario $S_1$ are not substantially reduced compared to scenario $S_2$ (Table 7). Thus we can conclude that the atmospheric $^{13}CH_4$ observations do not add a significant constraint on the methane emissions to the $CH_4$ mixing ratio measurements. This may be attributed to (1) the scarcity of atmospheric $^{13}CH_4$ observations compared to the $CH_4$ mixing ratio observations available including the lack of southern hemispheric $^{13}CH_4$ measurements during our target time period and (2) the uncertainties in the $^{13}CH_4$ content of the various $CH_4$ sources. The two exceptions are bogs and Siberian gas. Since they are both located at high northern latitudes, their signal in atmospheric $CH_4$ concentrations only differs from each other in its seasonality, but meridional $CH_4$ concentration gradients are similar. The different $^{13}C$ content of both sources thus significantly helps to discriminate between both sources. Since the source magnitudes in scenario $S_2$ are very similar to $S_1$, $S_2$ is not displayed in graphical form.

To investigate to what extent increased knowledge of isotopic characteristics of atmospheric methane and its sources and sinks would help to further restrict the atmospheric $CH_4$ budget, we run the inverse model, varying (1) uncertainties in $\delta^{13}CH_4$ measurements, (2) uncertainties in the $^{13}C$ content of sources and in the kinetic isotope effects, and (3) both uncertainties simultaneously. In this sensitivity study, the corresponding a priori uncertainties have been multiplied with a scaling factor $\gamma$. The (geometric) mean of the resulting squared a posteriori source uncertainties, expressed in percent of

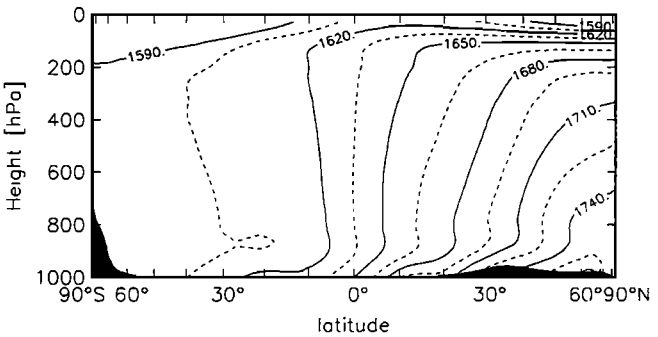


**Figure 7.** Simulated annual and zonal mean $CH_4$ concentrations in the base scenario $S_1$: isolines are 1620, 1650,..., 1800, 1900, 2000 ppbv (solid lines) and 1605, 1635,..., 1785, 1850, 1950 ppbv (dashed lines).

its a priori value, is plotted versus the scaling factor $\gamma$ in Figure 12.

It can be seen that a better knowledge of the $^{13}C$ content of $CH_4$ sources and fractionation factors alone does not help much to constrain the $CH_4$ source magnitudes. Lower uncertainties in atmospheric $\delta^{13}$ measurements alone would also be relatively inefficient in constraining $CH_4$ source magnitudes. A substantial improvement can only be obtained by reducing both uncertainties in the $\delta^{13}CH_4$ measurements and in the $^{13}C$ content of $CH_4$ sources and fractionation processes due to sinks simultaneously.

However, we did not investigate the effect of introducing additional $\delta^{13}CH_4$ measurement sites. More $\delta^{13}CH_4$ measurements, for example, in the southern hemisphere, are expected to increase the power of the isotopic data as constraints for $CH_4$ emission magnitudes, since the interhemispheric $\delta^{13}CH_4$ gradient is a prominent observational feature.

**7.2.2. 1986 winds (scenario $S_3$).** The use of ECMWF's analyzed wind fields based on one single year (1987) in the transport model could potentially influence the results. In scenario $S_3$, we performed a sensitivity study, in which wind fields from the year 1986 were used instead. The resulting modeled $CH_4$ mixing ratios at the NOAA/CMDL stations are included in Figure 6. Seasonal cycles are generally similar to those obtained in the base scenario ($S_1$). Smaller differences are apparent at particular months at some stations, for instance, at Mould Bay, Canada (in January, March, and December), at Point Barrow, Alaska (in January, March, and October), on the Azores (in December), at Cape Kumukahi, Hawaii (in January and February), on Guam (in February), and on Christmas Island (from January through April). They can be attributed to interannual differences in wind speed, wind direction, and vertical stability of the atmosphere in the region of these stations and nearby methane sources. At high northern latitudes, fluctuations in $CH_4$ mixing ratios can be attributed to the Siberian gas source, which is in the present simulations specified in a relatively small area. Hence interannual variations in atmospheric transport in the Siberian region substantially affect methane concentrations in high northern latitudes. The a posteriori $CH_4$ emission estimates resulting from the inverse model, driven with 1986 wind data, are given in Table 7

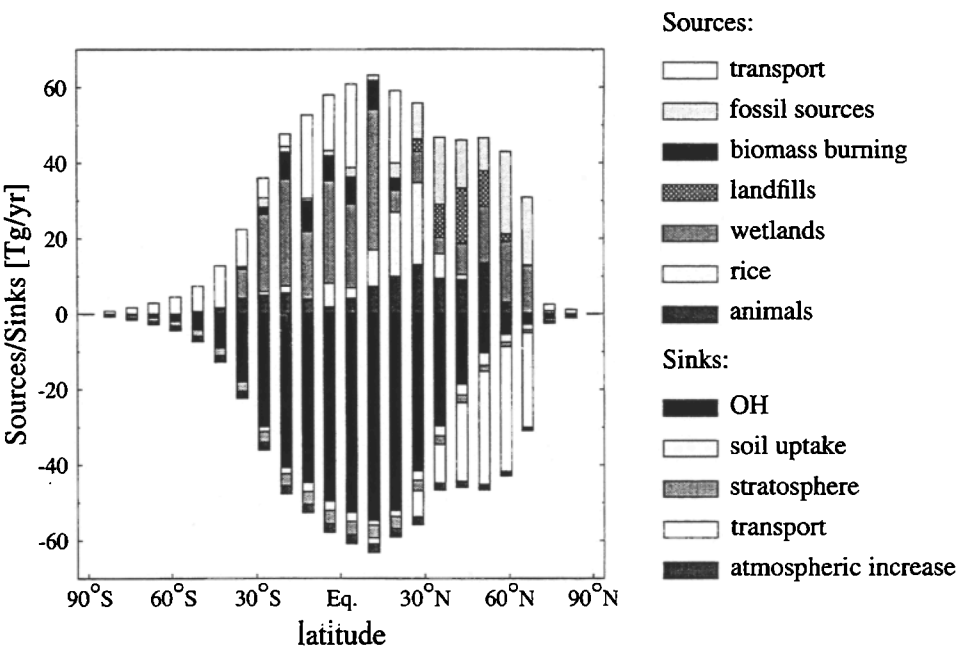


**Figure 8.** Simulated annual $CH_4$ budget (sources are displayed in a positive direction, sinks and the atmospheric increase term are displayed in a negative direction, and transport may be positive or negative) in each (7.8° wide) model latitude band in the base scenario $S_1$.

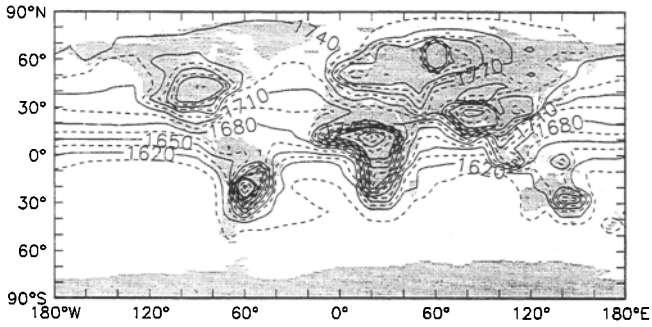


**Figure 9.** Simulated annual mean $CH_4$ concentrations in model level 1 (surface) in the base scenario $S_1$: isolines are 1600, 1650,..., 1800, 1900, 2000 ppbv (solid lines) and 1625, 1675,..., 1775, 1850, 1950, 2050 ppbv (dashed lines).

in the column labelled $S_3$ (1986 winds). It can be seen that a posteriori source magnitudes are quite similar to those of the base scenario ($S_1$). The main difference is a reduction of the biomass burning emissions compensated by a corresponding reduction in the OH sink. However, the differences from scenario $S_1$ are generally within the limits given by the stated uncertainties.

**7.2.3. Sensitivity of results to a priori estimates.** The main result of the inverse modeling approach is the reduction of the a priori uncertainties of the source magnitudes. In the base scenario $S_1$, the uncertainty of the emissions from rice paddies is reduced by more than 50%, the uncertainties of the biomass burning and wetland emissions are reduced by approximately 40%, the uncertainty of the landfill emissions is reduced by 25%, while the other source magnitude uncertainties (animals, coal, and total fossil sources) are not significantly reduced.

With two sensitivity studies, we investigated how this result depends on the a priori estimates of source magnitudes and their uncertainties. First, in scenario $S_6$ we choose a different set of a priori estimates of $CH_4$ sources based on the 1994 IPCC Scientific Assessment [*Prather et al.*, 1995], instead of those made by *Crutzen* [1995]. Several source magnitudes differ between both sets of estimates, with the largest difference being the contributions of wetlands. Crutzen estimated the natural $CH_4$ source based on preindustrial $CH_4$ levels known from measurements of air trapped in ice cores [*Nakazawa et al.*, 1993] assuming no significant changes in global mean OH concentrations and thus came up with an estimated wetland source of 270 ± 50 Tg/yr. The lower IPCC estimate is mainly based on flux measurements in the Amazon region and in high-latitude tundra regions. The a priori estimates based on IPCC together with a posteriori estimates resulting from the inverse model are listed in Table 9. Comparing scenario $S_6$ with $S_1$, the largest differences are found in the estimated wetland source. Applying the inverse model, the high a priori estimate of wetland emission made by *Crutzen* [1995] and the low estimate of *Prather et al.* [1995] tend to converge to intermediate values of 232 ± 27 Tg/yr and 193 ± 27 Tg/yr, respectively. The difference in the wetland source between both scenarios is fully attributed to the (predominantly tropical)

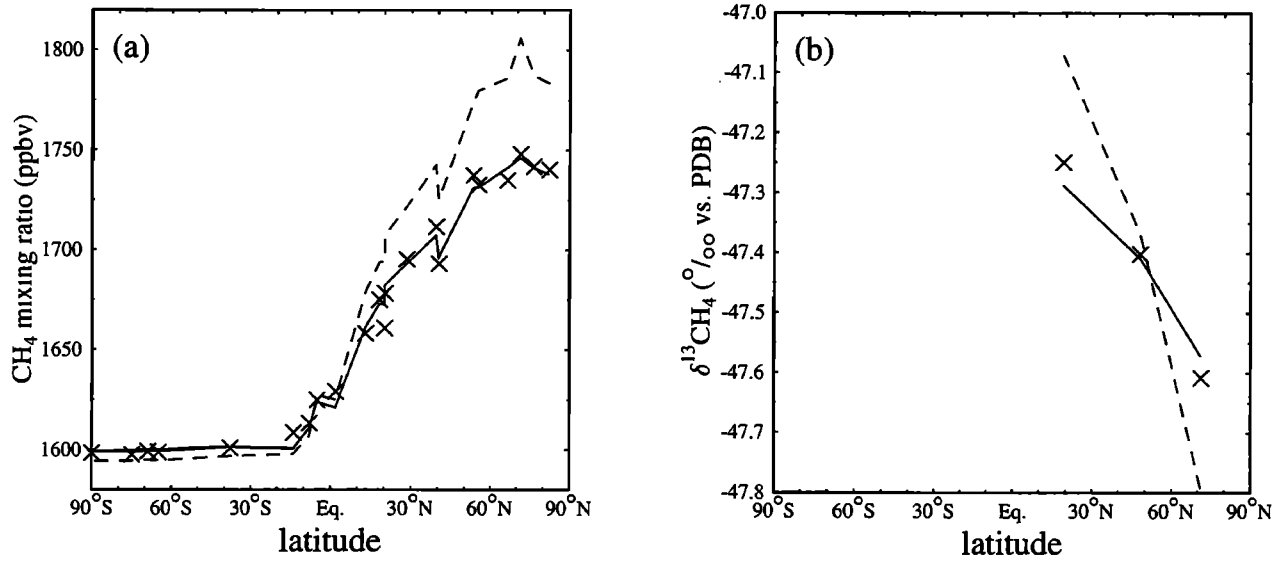


**Figure 10.** Annual mean meridional profile: (a) Simulated (solid line, base scenario; dashed line, a priori scenario) and observed (crosses, *Dlugokencky et al.* [1994c], and *Quay et al.* [1991]) annual mean $CH_4$ mixing ratios and (b) $\delta^{13}$C-$CH_4$ isotope ratios versus latitude at the observational stations. The apparent discontinuities in the simulated profiles reflect the fact that the stations are located at different longitudes and altitudes.

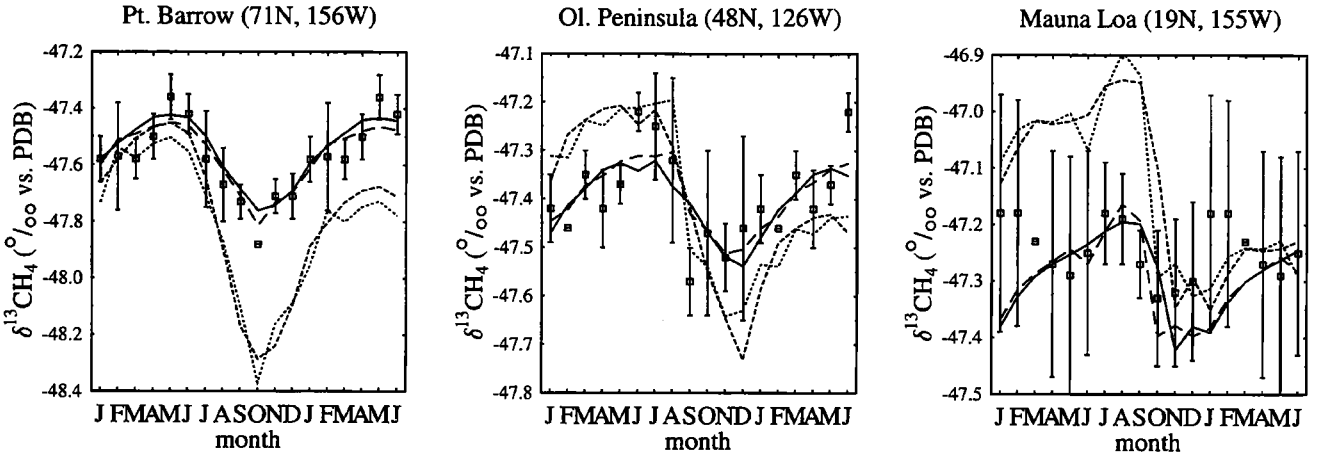


**Figure 11.** Simulated (dotted and solid lines, a priori scenario and scenario $S_1$ using 1987 wind data; short-dashed and long-dashed lines, a priori scenario and scenario $S_3$ using 1986 wind data in the transport model) and observed (squares with $1\sigma$ error bars) $\delta^{13}CH_4$ isotope ratios at the three available observational sites [*Quay et al.*, 1991]. The months of January to June are displayed twice in order to reveal the seasonal cycle more clearly.

swamps, whereas bogs, which are mainly located north of 50°N, have similar magnitudes in both scenarios. This difference is, on the other hand, mainly compensated by a corresponding reduction of the estimated OH sink from 469 Tg/yr in scenario $S_1$ to only 442 Tg/yr in scenario $S_6$. This simultaneous reduction in the $CH_4$ source from swamps and the OH sink, combined with some minor changes in the other sources, affects the modeled $CH_4$ mixing ratios only slightly, since both the swamp source and the OH sink peak in tropical regions and their atmospheric signals in the $CH_4$ mixing ratios at the observational sites nearly cancel each other.

This behavior reflects a principle difficulty of inverse modeling: the ill-conditioned nature of the inverse problem. This means that small uncertainties in the atmospheric observations are mapped (by the inverse model) onto much higher uncertainties in the source/sink estimates. The reason behind this is the fact that very different source/sink configurations may result in very similar modeled $CH_4$ mixing ratios, at least at the available stations which are located relatively far away from major sources. To demonstrate this, we rerun the inverse model with the a priori estimates from scenarios $S_1$ and $S_6$ but keeping the sink magnitudes constant at their a priori values. The resulting a posteriori source estimates are listed in the right columns of Tables 7 and 9 (scenarios $S_7$ and $S_8$, respectively). The predicted concentration differences between scenarios $S_6$ and $S_8$ are indeed small (not displayed), despite the fact that the sources and sinks show relatively large differences.

In the present NOAA/CMDL network, most stations are located far away from major source regions since the network was designed to monitor large-scale background air. Clearly, the numerical condition of the inverse problem would be much better if more stations downwind of major sources were available. However, other uncertainties would be enlarged. For instance, $CH_4$ mixing ratios at such stations are much more variable than at background stations and depend on local meteorological conditions which are often badly represented in coarse-grid atmospheric models.

With the notations of equation (14), the weighted mean squared deviation between modeled and observed $CH_4$ data $X^2$ is defined as

**Table 8.** A Priori $^{13}C$ Content of Atmospheric $CH_4$ Sources According to *Levin* [1994] and Kinetic Isotope Effects $(k_{13}/k_{12} - 1)$ of $CH_4$ Sinks and Their a Posteriori Estimates Obtained With the Inverse Model

| Source/Sink | A Priori | A Posteriori ($S_1$) |
|---|---|---|
| Animals | -62±3 | -61.8±2.9 |
| Rice | -63±3 | -62.8±2.9 |
| Bogs | -64±3 | -64.8±2.8 |
| Swamps | -59±5 | -58.7±3.3 |
| Landfills | -51±2 | -50.9±2.0 |
| Biomass burning | -25±3 | -25.0±3.0 |
| Coal | -35±3 | -34.9±3.0 |
| Siberian gas | -40±2 | -40.1±2.0 |
| Oil and other gas | -40±2 | -40.0±2.0 |
| Tropospheric OH | -5.4±0.9 | -5.4±0.8 |
| Stratosphere | -12±4 | -12.2±4.0 |
| Soil uptake | -21±10 | -21.8±9.6 |
| Atmospheric trend | 0±.06 | -.01±.05 |

Uncertainties represent 95% confidence intervals ($2\sigma$). All $\delta^{13}C$ values are expressed in per mil versus PeeDee Belemnite (PDB), the atmospheric trend in per mil per year. From *Cantrell et al.* [1990], *King et al.* [1989], and *Brenninkmeijer et al.* [1995].

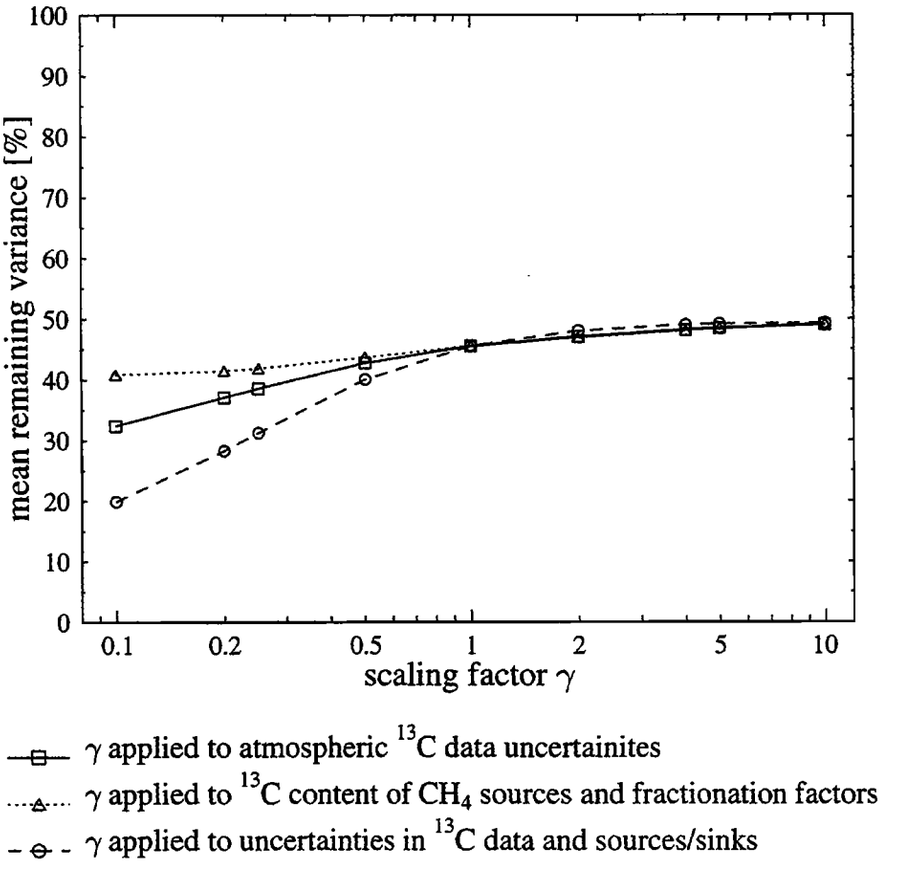


**Figure 12.** Reduction of $CH_4$ source uncertainties versus a scaling factor $\gamma$ for uncertainties in atmospheric $\delta^{13}CH_4$ measurements (solid line with squares) in $^{13}C$ content of methane sources and fractionation factors (dotted line with triangles) or in atmospheric $^{13}C$ data and $^{13}C$ contant of sources and fractionation factors simultaneously (dashed line with circles). The case $\gamma = 1$ corresponds to the base scenario $S_1$.

$$X^2 = \frac{1}{n_i} \cdot \sum_{i=1}^{n_i} s_i^{-2} \left(\chi_{\text{model},i} - \chi_{\text{obs},i}\right)^2 . \qquad (17)$$

As listed in the last line of Table 9, it increased only slightly from $S_6$ to $S_8$ because the increased differences at some tropical stations, in particular, at Mauna Loa (20°N), on Christmas Island (2°N), and in American Samoa (14°S) are to a large degree compensated by reduced differences at Antarctic stations due to a more realistic simulation of the seasonal amplitude in $CH_4$ mixing ratios at these stations.

In a further sensitivity study, we investigated how changes in the precision of atmospheric measurements and in the a priori estimated source/sink magnitudes alter the results of the inverse model. This was investigated by scaling the uncertainties assigned to the atmospheric $CH_4$ and $\delta^{13}CH_4$ observations and/or the a priori $CH_4$ source/sink magnitudes with an overall scaling factor $\gamma$. Analogous to section 7.2.1, we plot the mean remaining variance of the $CH_4$ source magnitude estimates after the inverse model was applied relative to their a priori values versus the scaling factor $\gamma$ (Figure 13). Clearly, in the hypothetical case of a much better a priori knowledge of source magnitudes (i.e., lower a priori uncertainties), our ability to further reduce uncertainties in source magnitude estimates by the inverse model would be much more limited.

In reality, a priori source magnitude estimates are, in contrast to the assumption in our modeling approach, not independent from each other and from the observed $CH_4$ concentrations (section 6.2 of this work). This implies that we might underestimate the a priori uncertainties of $CH_4$ source magnitude estimates. As can be seen from Figure 13, with higher a priori uncertainties of $CH_4$ sources, the atmospheric data would become more important to constrain source estimates, and the relative difference between the uncertainties of a priori and a posteriori source magnitude estimates would

**Table 9.** A Priori Methane Source and Sink Magnitude Estimates According to the 1994 Intergovernmental Panel on Climate Change (IPCC) Scientific Assessment and Corresponding a Posteriori Estimates Obtained with the Inverse Model for the Time Period 1983–1989

| Source/ Sink | A Priori (IPCC) | A Posteriori $S_6$ | A Posteriori $S_8$ (Sinks Fixed) |
|---|---|---|---|
| Animals[a] | 110±18 | 101±17 | 102±17 |
| Rice | 60±40 | 64±22 | 77±19 |
| Wetlands | 135±50 | 193±27 | 215±19 |
| Bogs | (40)[b] | 41±8 | 40±8 |
| Swamps | (95)[b] | 153±26 | 174±18 |
| Landfills | 65±43 | 38±22 | 40±21 |
| Biomass burning | 40±30 | 46±12 | 48±12 |
| Fossil sources | 100±25 | 100±21 | 102±21 |
| Coal | 35±15 | 30±15 | 30±15 |
| Siberian gas | (20)[b] | 33±14 | 32±13 |
| Oil and other gas | (45)[b,c] | 36±28 | 40±28 |
| Tropospheric OH | -480±96[d] (-407)[b,e] | -442±29 | -480[f] |
| Stratosphere | -40±8 | -42±8 | -40[f] |
| Soil uptake | -30±15 | -25±14 | -30[f] |
| Atmospheric increase | 33.38±0.8 | 33.6±0.8 | 33.5±0.8 |
| Total emissions | 510 | 542 | 584 |
| $X^2$ ($CH_4$ data only) | 2.33 | 0.90 | 0.92 |
| $X^2$ ($CH_4$ and $\delta^{13}$ data) | 2.20 | 0.90 | 0.91 |

Uncertainties represent 95% confidence intervals ($2\sigma$); units are in Teragrams per year, except for $X^2$, which is expressed in terms of $\sigma^2$.

[a]Including animal wastes.

[b]Values in parentheses were not used for inverse modeling but only applied in forward model calculations (see text).

[c]By difference (total fossil minus other fossil sources).

[d]Calculated with the three-dimensional transport-chemistry model TM2 in this study.

[e]Calculated from global $CH_4$ budget equation using given emission estimates.

[f]Fixed sink magnitudes.

be enlarged. Therefore, the calculated reduction of the average uncertainty of $CH_4$ source magnitudes of approximately one third obtained in the base scenario ($S_1$) indicates only a lower limit of the information gained from atmospheric observations. On the other hand, absolute uncertainties of the individual a posteriori $CH_4$ source magnitude estimates may be slightly underestimated.

As also shown in Figure 13, possible decreases in the uncertainties of atmospheric $CH_4$ and $\delta^{13}CH_4$ measurements lead to lower uncertainties in the methane source magnitudes estimated by the inverse model. For example, a 50% smaller data uncertainty ($\gamma = 0.5$) reduces the mean remaining variance of the source magnitudes from 46% to 28% of their a priori value. Further efforts to decrease the uncertainty of monthly mean $CH_4$ concentrations at measurement sites, for instance, by higher sample frequencies or quasi-continous in situ measurements [*Dlugokencky et al.*, 1995], as well as efforts to increase the number of properly chosen measurement sites, could therefore be highly valuable for the understanding of the atmospheric methane cycle.

### 7.3. Differences Between the 1980s and the 1991–1993 Target Time Period (Scenarios $S_4$, $S_5$)

The rate of increase of atmospheric $CH_4$ mixing ratios slowed down during the 1980s [*Steele et al.*, 1992], and an even more dramatic decrease in its growth rate occurred in the early 1990s [*Dlugokencky et al.*, 1994b]. The reason for this behavior, whether due to changes in sources, in sinks, or a combination of both, is not understood. In this study, we restricted ourselves to the question of whether this decrease in the atmospheric methane growth rate could be associated with changes in particular sources, provided that the methane lifetime did not change. Therefore we performed an inverse model run in which we used atmospheric $CH_4$ data from the time period 1991–1993 (scenario $S_5$) and compared it to our results obtained for 1983–1989. Since four of

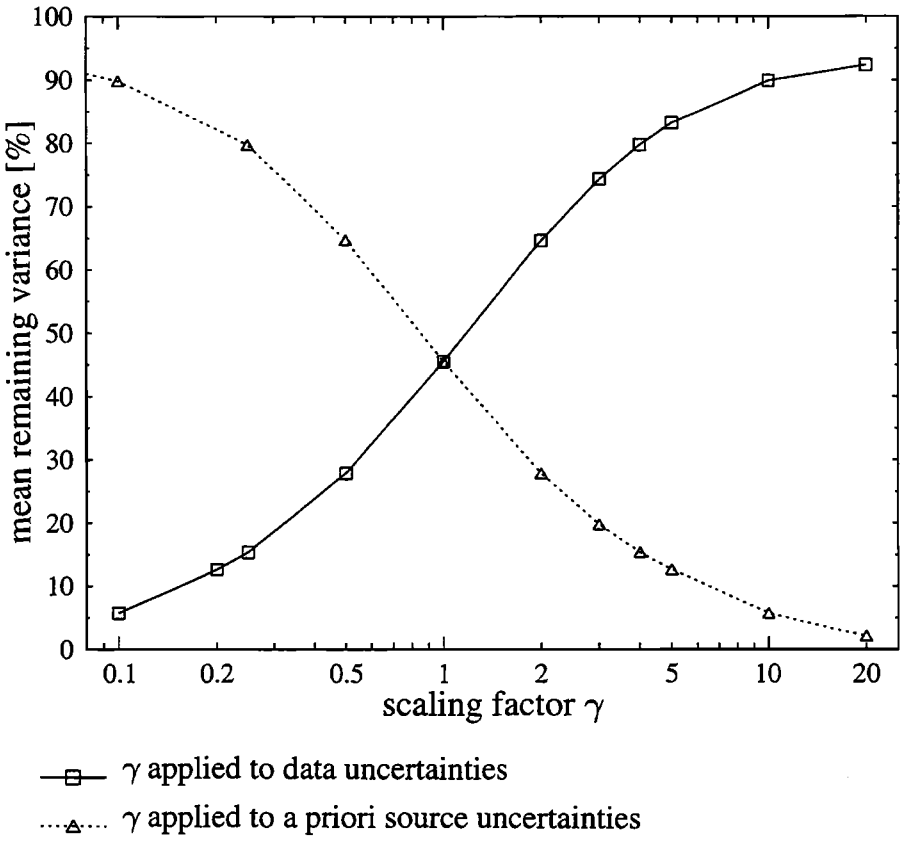


**Figure 13.** Reduction of $CH_4$ source uncertainties versus a scaling factor $\gamma$ for uncertainties in atmospheric $CH_4$ and $\delta^{13}CH_4$ measurements (solid line with squares) or in a priori source magnitude estimates (dotted line with triangles). The case $\gamma = 1$ corresponds to the base scenario $S_1$.

the observational sites used in the base scenario calculations (those on the Azores, Virgin Islands, Amsterdam Island, and Halley Bay in Antarctica) were not measuring methane during a sizeable fraction of the 1991–1993 time period, we could only use 18 NOAA/CMDL stations in this calculation. To allow for a sound comparison, we also repeated the calculation for the target time period 1983–1989 with these 18 stations (and the $\delta^{13}CH_4$ data) only (scenario $S_4$).

Since we assumed no variation in $CH_4$ lifetime between both target time periods, sink magnitudes in scenario $S_5$ were fixed in order to match the $CH_4$ lifetime resulting from scenario $S_4$. Because of increased $CH_4$ concentrations in 1991–1993, however, absolute sink magnitudes should have also increased since the 1983–1989 target time period. This effect overcompensates the effect of the reduced atmospheric growth rate, leading to a slightly higher total $CH_4$ emission estimate of 587 Tg/yr in 1991–1993 compared to 577 Tg/yr in 1983–1989 Table 10. A similar increase in total $CH_4$ sources of 1.4 Tg/yr$^2$ has also been calculated by *Prinn et al.* [1992] assuming no changes in $CH_4$ lifetime during the time period 1983–1990. However, the difference in total $CH_4$ emissions estimated for 1983–1989 and 1991–1993 is small compared to the uncertainties of the individual source magnitudes.

A remarkable difference between scenarios $S_4$ and $S_5$ is the decrease in estimated Siberian gas emissions from 37 ± 15 Tg/yr to 17 ± 14 Tg/yr (Table 10). Since we used the same a priori estimate of total fossil sources (100 ± 18 Tg/yr) for both target time periods, the calculated $CH_4$ emissions from oil/other gas, on the other hand, increase from 31 ± 24 Tg/yr to 46 ± 23 Tg/yr. To balance the global $CH_4$ budget, the inverse model yields increased emissions from rice paddies (88 ± 20 Tg/yr in 1991–1993 compared to 70 ± 24 Tg/yr in 1983–1989), whereas all other source magnitude estimates do not change much. However, such an enormeous increase in $CH_4$ emissions from rice paddies can hardly be believed to be real, probably pointing to limitations in the reliability of the inverse model when applied to the target time period 1991–1993. These problems may arise from the fact that the methane growth rate shows a high temporal and interhemispheric variability during these three years [*Dlugokencky et al.*, 1994b, 1995]. Hence the assumption that the atmospheric $CH_4$ cycle was in

**Table 10.** A Priori and a Posteriori Methane Source and Sink Magnitude Estimates for the Two Time Periods 1983–1989 and 1991–1993

| Source/ Sink | A Priori [*Crutzen*, 1995] | A Posteriori $S_4$ (1983–1989) | A Posteriori $S_5$ (1991-1993) |
|---|---|---|---|
| Animals[a] | 110±22 | 91±20 | 90±20 |
| Rice | 80±60 | 70±24 | 88±20 |
| Wetlands | 270±50 | 234±28 | 237±20 |
| Bogs | (100)[b] | 44±8 | 44±7 |
| Swamps | (170)[b] | 190±26 | 192±19 |
| Landfills | 40±20 | 37±16 | 35±15 |
| Biomass burning | 40±20 | 43±11 | 40±12 |
| Fossil sources | 100±18 | 102±16 | 97±15 |
| Coal | 35±10 | 33±10 | 35±10 |
| Siberian gas | (20)[b] | 37±15 | 17±14 |
| Oil and other gas | (45)[b,c] | 31±24 | 46±23 |
| Tropospheric OH | -480±96[d] (-530)[b] | -471±39 | -489[e] |
| Stratosphere | -40±8 | -44±8 | -46[e] |
| Total emissions | 640 | 577 | 587 |
| $X^2$ ($CH_4$ data only) | | 0.97 | 0.94 |
| $X^2$ ($CH_4$ and $\delta^{13}$ data) | | 0.96 | 0.93 |

Uncertainties represent 95% confidence intervals ($2\sigma$); units are in Teragrams per year, except for $X^2$, which is expressed in terms of $\sigma^2$.

[a]Including animal wastes.

[b]Values in parentheses were not used for inverse modeling but only applied in forward model calculations (see text).

[c]By difference (total fossil minus other fossil sources).

[d]Calculated with the three-dimensional transport-chemistry model TM2 in this study.

[e]Calculated from $S_4$ assuming constant methane lifetime during both target periods; absolute values are higher than in $S_4$ since average atmospheric methane mixing ratios have been growing from 1651 ppbv in 1986 to 1714 ppbv in 1992.

a quasi steady state is not a very good approximation during the period 1991–1993. Nevertheless, our results support the conclusion of *Dlugokencky et al.* [1994a, b] that the decrease in the $CH_4$ growth rate between 1984 and 1992 may be driven by changes in the region north of 30°N, probably in the Siberian gas industry or coal mining in the former Soviet Union. However, it is important to note that the apparent changes in source estimates between scenarios $S_4$ and $S_5$ are not exceeding the stated uncertainties and are thus not statistically significant (on the 95% confidence interval). In addition, our assumption that $CH_4$ lifetime did not change between both target time periods is also somewhat speculative. Hence the question as to which sources might have changed during the last decade cannot uniquely be answered on the basis of the present inverse model.

The sudden reduction in the $CH_4$ growth rate observed in 1992/1993 can, of course, only be explained by sudden changes in sources and/or sinks. Since we always used multiyear averages of measured data and are, consequently, only able to simulate average states of the atmospheric methane cycle over the multiyear target time periods, such sudden changes can not be addressed with the inverse model in its present form. Effects of possible changes in atmospheric transport are also beyond the scope of this study, where the atmospheric transport always employs meteorological data from the years 1986 and 1987.

## 8. Conclusions

We applied an inverse modeling method on the global atmospheric $CH_4$ cycle in order to investigate the extent to which the available measurements of atmospheric $CH_4$ mixing ratios and isotope ratios constrain large-scale atmospheric $CH_4$ sources. We confirmed the result of *Fung et al.* [1991], who concluded that it is possible to construct scenarios of global methane sources which reproduce the main features seen in the NOAA/CMDL methane observations. Additionally, the few available atmospheric $^{13}C/^{12}C$ isotope ratio measurements are also well simulated.

The inverse modeling approach applied in this study enables an objective treatment of the uncertainties of

the source and sink magnitudes and allows us to investigate the extent to which the atmospheric observations constrain the source and sink magnitudes. Since we ignored that a priori source magnitude estimates are already influenced by information obtained from atmospheric $CH_4$ concentration measurements, we can only give a lower limit for the average reduction of source magnitude estimates inferred from atmospheric observations. On the other hand, the absolute a posteriori uncertainties of source magnitudes calculated by the inverse model may be slightly underestimated. The inverse modeling approach enabled an objective determination of the range of methane emissions which are consistent with the atmospheric observations. This is the main advantage of this inverse method compared to the approach of *Fung et al.* [1991] who were only able to, subjectively, select several source/sink configurations and check them for consistency with the observations. Nevertheless, the conclusions of *Fung et al.* [1991] and this study are in remarkably good agreement. The method applied in this study substantially differs from the approach of *Brown* [1993, 1995] who did not use any a priori information on the location and seasonality of $CH_4$ sources. Furthermore, they performed their calculations with a two-dimensional transport model, thereby ignoring any longitudinal variability of $CH_4$ sources, sinks, and atmospheric concentrations. We assume that this significantly reduces the power of atmospheric observations for deducing $CH_4$ emissions. We also confirmed the result of *Fung et al.* [1991] that it is not uniquely possible to select only one single source/sink configuration. Furthermore, we can conclude that the atmospheric observations do reduce the uncertainties of estimated methane source magnitudes by at least one third, with highest uncertainty reductions for rice paddies, wetlands, biomass burning, and landfills. The uncertainty of the estimated $CH_4$ emission magnitude from animals could not be reduced significantly. This is also found for the fossil fuel related $CH_4$ emissions, which are constrained by the global $^{14}CH_4$ budget. The uncertainty in methane lifetime, predominantely determined by uncertainties in the calculated global mean OH concentrations, also contributes to the uncertainties in $CH_4$ emission estimates. Overall, it can be concluded that scenarios $S_1$ and $S_6$ are both capable of adequately simulating the main features seen in the NOAA/CMDL $CH_4$ and the available $\delta^{13}CH_4$ observations.

We could demonstrate that the ill-conditioned nature of the inverse problem constitutes a principal difficulty in constraining $CH_4$ emissions from measured atmospheric mixing ratios. The reason behind this is the fact that substantially differing source/sink configurations do not necessarily lead to substantial differences in modeled methane mixing ratios at the present observational network sites. Therefore small uncertainties in the observational data correspond to much higher uncertainties in the estimated emission magnitudes.

The choice of a particular base year for the meteorological input data used in the transport model TM2 apparently does not strongly influence the results of the inverse model. Nevertheless, in further studies we plan to use wind data based on each particular year to be simulated rather than averaging the status of the atmospheric methane cycle over a multiyear target time period. Of course, this will substantially increase the required computational resources.

Clearly, the available data on the geographical and temporal variability of the $CH_4$ sources and sinks strongly influence the results of a synthesis inversion study. We demonstrated this by lagging the time dependence of the temperature controlled $CH_4$ emissions from bogs by 2 months. This led to a substantially improved agreement of the seasonal cycle of modeled and observed atmospheric $CH_4$ mixing ratios at high northern latitudes. However, we did not attempt in this study to systematically quantify the uncertainties in $CH_4$ source magnitude estimates arising from erroneous information on the geographical and temporal variability of all methane sources and sinks.

The limited amount of atmospheric $^{13}CH_4$ observations does not significantly constrain most methane emission magnitudes. However, they are helpful to discriminate between $CH_4$ emissions from bogs and Siberian gas, the two major sources at high northern latitudes. With more atmospheric $\delta^{13}CH_4$ measurements available, and the assessment of the $^{13}CH_4$ content of the various $CH_4$ sources and the kinetic isotope effects of its sinks being improved, the isotopic $\delta^{13}CH_4$ data might be much more useful in constraining the global atmospheric $CH_4$ budget.

## Appendix

The continuty equation (1) for $^{13}CH_4/^{12}CH_4$ isotope ratios has the form

$$T[\rho(x,t)\chi_{\text{model}}(x,t)R(x,t)] = -\lambda_{OH}(x,t)(1+\epsilon)\rho(x,t)\chi_{\text{model}}(x,t)R(x,t) + \sum_{j=1}^{n} Q_j(x,t)R_j, \quad \text{(A1)}$$

where the notations of equation (7) apply, $R$ and $R_j$ denote the $^{13}C/^{12}C$ isotope ratios of atmospheric methane and methane sources, respectively, and $\epsilon$ ($= k_{13}/k_{12} - 1$) describes the kinetic isotope effect of the reaction with OH. Substracting the continuty equation (7), multiplied with an arbitrary reference isotope ratio $R_{\text{ref}}$, yields

$$T[\rho(x,t)\chi_{\text{model}}(x,t)(R(x,t)-R_{\text{ref}})]$$
$$= -\lambda_{\text{OH}}(x,t)(1+\epsilon)\rho(x,t)\chi_{\text{model}}(x,t)(R(x,t)-R_{\text{ref}}) + \sum_{j=1}^{n} Q_j(x,t)(R_j - R_{\text{ref}}). \quad \text{(A2)}$$

Applying abbreviation (8) and the usual $\delta$ notation,

$$R(x,t) = (1+\delta(x,t))R_{\text{PDB}}, \quad \text{(A3a)}$$

$$R_{\text{ref}} = (1+\delta_{\text{ref}})R_{\text{PDB}}, \quad \text{(A3b)}$$

and

$$R_j = (1+\delta_{\text{q,j}})R_{\text{PDB}}, \quad \text{(A3c)}$$

where $R_{\text{PDB}}$ denotes the PeeDee Belimnite (PDB) Carbonate Standard of approximately 0.0112372 [*Craig*, 1957], this is equivalent to

$$T[\rho(x,t)\chi_{\text{model}}(x,t)(\delta(x,t)-\delta_{\text{ref}})]$$
$$= Q_0(x,t)((1+\epsilon)(1+\delta(x,t))-(1+\delta_{\text{ref}})) + \sum_{j=1}^{n} Q_j(x,t)(\delta_{\text{q,j}} - \delta_{\text{ref}}). \quad \text{(A4)}$$

We set $\delta_{\text{ref}}$ (up to now arbitrary) to the global mean atmospheric $\delta^{13}CH_4$ value $\delta_{\text{atm}}$ and approximate in the $Q_0$ term,

$$(1+\epsilon)(1+\delta(x,t)) \approx (1+\epsilon)(1+\delta_{\text{atm}}) \approx 1+\delta_{\text{atm}}+\epsilon. \quad \text{(A5)}$$

Hence (A4) can be written in the form

$$T[\rho(x,t)\chi_{\text{model}}(x,t)(\delta(x,t)-\delta_{\text{atm}})]$$
$$= Q_0(x,t)\epsilon + \sum_{j=1}^{n} Q_j(x,t)(\delta_{\text{q,j}} - \delta_{\text{atm}}). \quad \text{(A6)}$$

For convenience, the further abbreviations $\Delta_0 = \epsilon$ and $\Delta_j = \delta_{\text{q,j}} - \delta_{\text{atm}}$ $(j = 1,\ldots,n)$ may be introduced. Together with definition (9), this leads to

$$T[\rho(x,t)\chi_{\text{model}}(x,t)(\delta(x,t)-\delta_{\text{atm}})] = \sum_{j=0}^{n} \Delta_j \alpha_j \hat{Q}_j(x,t). \quad \text{(A7)}$$

Since the deviation of the atmospheric $CH_4$ mixing ratio $\chi_{\text{model}}(x,t)$ from its global mean value $\chi_{\text{atm}}$ is small (generally less than 5% of $\chi_{\text{atm}}$, except for few grid points directly at strong sources), $\chi_{\text{model}}(x,t)$ can be approximated by $\chi_{\text{atm}}$ yielding

$$T[\rho(x,t)\chi_{\text{atm}}(\delta(x,t)-\delta_{\text{atm}})] = \sum_{j=0}^{n} \Delta_j \alpha_j \hat{Q}_j(x,t), \quad \text{(A8)}$$

or, equivalently,

$$T[\rho(x,t)(\delta(x,t)-\delta_{\text{atm}})] = \sum_{j=0}^{n} \frac{\Delta_j \alpha_j}{\chi_{\text{atm}}} \hat{Q}_j(x,t). \quad \text{(A9)}$$

Similar to the case of $CH_4$ concentrations (equation (10)), (A9) can thus be solved by

$$\delta(x,t) - \delta_{\text{atm}} = \sum_{j=0}^{n} \frac{\Delta_j \alpha_j}{\chi_{\text{atm}}} \chi_j(x,t) + \Delta_{00}, \quad \text{(A10)}$$

where the $\chi_j$ $(j = 0,\ldots,n)$ denote the solutions of equations (12) and $\Delta_{00}$ represents the initialization with a globally uniform $^{13}CH_4/^{12}CH_4$ isotope ratio.

It is important to note that, in the case of a trace gas with sudden big changes in magnitude or isotopic composition of its sources, the approximation made in equation (A8) could lead to substantial errors in modeling isotope ratios (*Tans*, 1997). However, in the case of the global methane cycle, this error is small compared to the uncertainties of the isotopic composition of the different sources and fractionation processes and the limitations arising from the scarcity of available atmospheric measurements of $^{13}CH_4/^{12}CH_4$ isotope ratios.

**Acknowledgments.** It is a pleasure to thank all the colleagues who provided us with helpful information and suggestions on many aspects of this study, among them P. Bergamaschi, C. Brenninkmeijer, M. Kanakidou, J. Lelieveld, and P. Zimmermann. Special thanks go to C. Brühl, F. Dentener, and E. Maier-Reimer for their help with photolysis rates, $N_2O_5$ removal coefficients, and $CH_3CCl_3$ ocean uptake rates, respectively. For valuable comments on earlier versions of the manuscript, we acknowledge M. Lawrence and S. Seitz. We also thank two anonymous reviewers for their helpful comments. P. Tans is gratefully acknowledged for his constructive review of the manuscript, in particular for clarifying remarks regarding the treatment of isotope ratios in the model. We also thank the Deutscher Wetterdienst (DWD) in Offenbach for providing us with the meteorological analyses of the ECMWF. This work was supported by the German Bundesministerium für Bildung, Wissenschaft, Forschung und Technologie (BMBF) as part of the Klimaschwerpunkt "Spurenstoffkreisläufe."

## References

Arpe, K., The hydrological cycle in the ECMWF short range forecasts, *Dyn. Atmos. Oceans*, *16*, 33–59, 1991.

Aselmann, I., and P.J. Crutzen, Global distribution of natural freshwater wetlands and rice paddies, their net primary productivity, seasonality and possible methane emissions, *J. Atmos. Chem.*, *8*, 307–358, 1989.

Bingemer, H.G. and P.J. Crutzen, The production of methane from solid wastes, *J. Geophys. Res.*, *92*(D), 2181–2187, 1987.

Brenninkmeijer, C.A.M., D.C. Lowe, M.R. Manning, R.J. Sparks, and P.F.J. van Velthoven, The $^{13}C$,$^{14}C$, and $^{18}O$ isotopic composition of CO, $CH_4$, and $CO_2$ in the higher southern latitudes lower stratosphere, *J. Geophys. Res.*, *100*(D), 26,163–26,172, 1995.

Brost, R., and M. Heimann, The effect of the global background on a synoptic-scale simulation of tracer concentration, *J. Geophys. Res., 96*(D), 15,415–15,425, 1991.

Brown, M.K.M., Deduction of emissions of sources gases using an objective inversion algorithm and a chemical transport model, *J. Geophys. Res., 98*(D), 12,639–12,660, 1993.

Brown, M.K.M., The singular value decomposition method applied to the deduction of the emissions and the isotopic composition of atmospheric methane, *J. Geophys. Res., 100*(D), 11,425–11,446, 1995.

Brühl, C., and P.J. Crutzen, MPIC two-dimensional model, NASA Ref. Publ. 1292, 103–104, 1993.

Butler, J.H., J.W. Elkins, T.M. Thompson, B.D. Hall, T.H. Swanson, and V. Koropalov, Oceanic Consumption of $CH_3CCl_3$: Implications for tropospheric OH, *J. Geophys. Res., 96*(D), 22,347–22,355, 1991.

Cantrell, A.C., R.E. Shetter, A.H. McDaniel, J.G. Calvert, J.A. Davidson, D.C. Lowe, S.C. Tyler, R.J. Cicerone, and J.P. Greenberg, Carbon kinetic isotope effect in the oxidation of methane by the hydroxyl radical, *J. Geophys. Res., 95*(D), 22,455–22,462, 1990.

Craig, H., Isotopic standards for carbon and oxygen and correction factors for mass-spectrometric analysis of carbon dioxide, *Geochim. Cosmochim. Acta, 12*, 133–149, 1957.

Crutzen, P.J., The role of methane in atmospheric chemistry and climate, in *Ruminant Physiology: Digestion, Metabolism, Growth and Reproduction: Proceedings of the Eighth International Symposium on Ruminant Physiology*, edited by W.v. Engelhardt, S. Leonhardt-Marek, G. Breves, and D. Giesecke, pp. 291–315, Ferdinand Enke Verlag, Stuttgart, Germany, 1995.

Crutzen, P.J., and P.H. Zimmermann, The changing photochemistry of the troposphere, *Tellus, Ser. A and B, 43*, 136–151, 1991.

Crutzen, P.J., I. Aselmann, and W. Seiler, Methane production by domestic animals, wild ruminants, other herbivorous fauna, and humans, *Tellus, Ser. B, 38*, 271–284, 1986.

Darmstädter, J., L.W. Ayres, R.U. Ayres, W.C. Clark, R.P. Crosson, P.J. Crutzen, PT.E. Graedel, R. McGill, J.F. Richards, and J.A. Torr, Impacts of world development on selected characteristics of the atmosphere: An integrated approach, Oak Ridge Nat. Lab. Rep., *ORNL/Sub/86 - 22033/1/V2*, 1987.

DeMore, W.B., S.P. Sander, D.M. Golden, R.F. Hampson, M.J. Kurylo, C.J. Howard, A.R. Ravishankara, C.E. Kolb, and M.J. Molina, Chemical kinetics and photochemical data for use in stratospheric modeling – Evaluation number 10, *JPL Publ. 92-20*, 1992.

Dentener, F., Heterogenous chemistry in the troposphere, Ph.D. thesis, Fac. Natuur- en Sterrenkunde, Univ. Utrecht, Utrecht, Netherlands, 1993.

Dentener, F., and P.J. Crutzen, Reaction of $N_2O_5$ on tropospheric aerosols: Impact on the global distributions of $NO_x$, $O_3$, and OH, *J. Geophys. Res., 98*(D), 7149–7163, 1993.

Dianov-Klokov, V.I., and L.N. Yurganov, A spectroscopic study of the global space-time distribution of atmospheric carbon monoxide, *Tellus, 33*, 262–273, 1981.

Dianov-Klokov, V.I, L.N. Yurganov, E.I. Grecho, and A.V. Dzhola, Spectroscopic measurements of atmospheric carbon monoxide and methane, 1, Latitudinal distribution, *J. Atmos. Chem., 8*, 139–151, 1989.

Dlugokencky, E.J., K.A. Masarie, P.M. Lang, P.P. Tans, L.P. Steele, and E.G. Nisbet, A dramatic decrease in the growth rate of atmospheric methane in the northern hemisphere during 1992, *Geophys. Res. Lett., 21*, 45–48, 1994a.

Dlugokencky, E.J., L.P. Steele, P.M. Lang, and K.A. Masarie, The growth rate and distribution of atmospheric methane, *J. Geophys. Res., 99*(D), 17,021–17,043, 1994b.

Dlugokencky, E.J., P.M. Lang, K.A. Masarie, and L.P. Steele, Atmospheric $CH_4$ records from sites in the NOAA/CMDL air sampling network, in *Trends '93: A Compendium of Data on Global Change*, edited by T.A. Boden, D.P. Kaiser, R.J. Sepanski, and F.W. Stoss, Rep. ORNL/CDIAC-65, pp. 274–350, Carbon Dioxide Inf. Anal. Cent., Oak Ridge Nat. Lab., Oak Ridge, Tenn., 1994c.

Dlugokencky, E.J., L.P. Steele, P.M. Lang, and K.A. Masarie, Atmospheric methane at Mauna Loa and barrow observatories: Presentation and analysis of in situ measurements, *J. Geophys. Res., 100*(D), 23,103–23,113, 1995.

Dörr, H., L. Katruff, and I. Levin, Soil texture parametrization of the methane uptake In aerated soils, *Chemosphere, 26*, 697–713, 1993.

Enting, I.G., Inverse problems in atmospheric constituent studies, III, Estimating errors in surface sources, *Inverse Probl., 9*, 649–665, 1993.

Enting, I.G., C.M. Trudinger, R.J. Francey, and H. Granek, Synthesis inversion of atmospheric $CO_2$ using the GISS tracer transport model, Div. of Atmos. Res. *Tech. Pap. 29*, Commonw. Sci. and Ind. Res. Organ., Melbourne, Australia, 1993.

Fortuin, J.P., and U. Langematz, An update on the global ozone climatology and on concurrent ozone and temperature trends, in *Atmospheric Sensing and Modelling*, Proc. SPIE Ser., vol. 2311, edited by R.P. Santer, Washington, D.C., pp. 207–216, 1994.

Franzlau, E., and C.J. Popp, Nitrogen oxides produced from lightning, *J. Geophys. Res., 94*(D), 11,089–11,104, 1989.

Fung, I., J. John, J. Lerner, E. Matthews, M. Prather, L.P. Steele and P.J. Fraser, Three-dimensional model synthesis of the global methane cycle, *J. Geophys. Res., 96*(D), 13,033–13,065, 1991.

Galbally, I.E. and C.R. Roy, Destruction of ozone at the Earth's surface, *Q. J. R. Meteorol. Soc., 106*, 599–620, 1980.

Gossett, J.M., Measurements of Henry's law constants for $C_1$ and $C_2$ chlorinated hydrocarbons, *Environ. Sci. Technol., 21*, 202–208, 1987.

Hao, W.M., M.-H. Liu, and P.J. Crutzen, Estimates of annual and regional releases of $CO_2$ and other trace gases to the atmosphere from fires in the tropics, based on the FAO statistics for the period 1975–1980, in *Fire in the Tropical Biota, Ecological Studies*, vol. 84, edited by J. G. Goldammer, pp. 440–462, Springer-Verlag, New York, 1990.

Heimann, M., The global atmospheric tracer model TM2, *Tech. Rep. 10*, Deutsches Klimarechenzentrum, Hamburg, Germany, 1995.

Heimann, M., and C.D. Keeling, A three-dimensional model of atmospheric $CO_2$ transport based on observed winds, Model description and simulated tracer experiments, in *Aspects of Climate Variability in the Pacific and the Western Americas, Geophys. Monogr.*, Ser., vol. 55, edited by D. H. Peterson, pp. 237–275, AGU, Washington, D. C., 1989.

Heimann, M., P. Monfray, and G. Polian, Modeling the long-range transport of Rn-222 to subantarctic and antarctic areas, *Tellus, Ser. B, 42*, 83–99, 1990.

Hein, R., Inverse Modellierung des atmosphärischen Methan-Kreislaufs unter Verwendung eines drei-dimensionalen

Modells des Transports und der Chemie der Troposphäre, Ph.D. thesis, Fachbereich Geowissenschaften der Univ. Hamburg, Hamburg, Germany, 1994.

Hein, R., and M. Heimann, Determination of global scale emissions of atmospheric methane using an inverse modelling method, in *Non-$CO_2$ Greenhouse Gases*, edited by J. van Ham et al., pp. 271–281, Kluwer Acad. Publishers, Norwell, Mass., 1993.

Jaeger, L., Monatskarten des Niederschlags für die ganze Erde, *Ber. Dtsch. Wetterdienst, 139*, 1–38, 1976.

Jeffers, P.M., L.M. Ward, L.M. Woytowitch, and N.L. Wolfe, Homogeneous hydrolysis rate constants for selected chlorinated methanes, ethanes, ethenes, and propanes, *Environ. Sci. Technol., 23*, 965–969, 1989.

Junge, C.E., and P.E. Gustafson, On the distribution of sea salt over the United States and its removal by precipitation, *Tellus, 9*, 164–173, 1957.

Kanakidou, M., F.J. Dentener, and P.J. Crutzen, A global three-dimensional study of the fate of HCFCs and HFC-134a in the troposphere, *J. Geophys. Res., 100*(D), 18,781–18,801, 1995.

Kawa, S.R., and R. Pearson Jr., Ozone budgets from the dynamics and chemistry of marine stratocumulus experiment, *J. Geophys. Res., 94*(D), 9809–9817, 1989.

Keeling, C.D., R.B. Bacastow, A.F. Carter, S.C. Piper, T.P. Whorf, M. Heimann, W.G. Mook, and H. Roeloffzen, A three-dimensional model of atmospheric CO2 transport based on observed winds, 1, Analysis of observational data, in *Aspects of Climate Variability in the Pacific and Western Americas*, Geophys. Monogr., Ser., vol. 55, edited by D. H. Peterson, pp. 165–236, AGU, Washington, D. C., 1989.

King, S.L., P.D. Quay, and J.M. Landsdown, $^{13}C/^{12}C$ kinetic isotope effect for soil oxidation of methane at ambient atmospheric concentrations, *J. Geophys. Res., 94*(D), 18,273–18,278, 1989.

Kunz, C., Carbon-14 discharge at three light-water reactors, *Health Phys., 49*, 25–35, 1985.

Lang, P.M., L.P. Steele, R.C. Martin, and K.A. Masarie, Atmospheric methane data for the period 1983-1985 from the NOAA/GMCC global cooperative flask sampling network, *NOAA Tech. Memo. ERL CMDL-1*, Nat. Oceanic and Atmos. Admin. Environ. Res. Lab., Boulder, Colo., 1990a.

Lang, P.M., L.P. Steele, and R.C. Martin, Atmospheric methane data for the period 1986-1988 from the NOAA/CMDL global cooperative flask sampling network, *NOAA Tech. Memo. ERL CMDL-2*, Nat. Oceanic and Atmos. Admin. Environ. Res. Lab., Boulder, Colo., 1990b.

Lassey, K.R., D.C. Lowe, C.A.M. Brenninkmeijer, and A.J. Gomez, Atmospheric methane and its carbon isotopes in the southern hemisphere: Their time series and an instructive model, *Chemosphere, 26*, 95–109, 1993.

Lawrence, M.G., W.L. Chameides, P.S. Kasibhatla, H. Levy II, and W. Moxim, Lightning and atmospheric chemistry: The rate of atmospheric NO production, in *Handbook of Atmospheric Electrodynamics*, vol. 1, edited by H. Volland, pp. 197–211, CRC Press, Boca Raton, Fla., 1995.

Lerner, J., E. Matthews, and I. Fung, Methane emissions from animals: A global high-resolution database, *Global Biogeochem. Cycles, 2*, 139–156, 1988.

Levin, I., The recent state of carbon cycling through the atmosphere, in *Carbon Cycling in the Glacial Ocean: Constraints on the Ocean's Role in Global Change*, edited by R. Zahn, pp. 3–13, Springer-Verlag, New York, 1994.

Levy, H., II, and W.J. Moxim, Simulated global distribution and deposition of reactive nitrogen emitted by fossil fuel combustion, *Tellus, Ser. B, 41*, 256–271, 1989.

Levy, H., II, J.D. Mahlmann, W.J. Moxim, and S.C. Liu, Troposheric ozone: The role of transport, *J. Geophys. Res., 90*(D), 3753–3772, 1985.

Lind, J.A., and G.L. Kok, Henry's law determinations for aqueous solutions of hydrogen peroxide, methylhydroperoxide, and peroxyacetic acid, *J. Geophys. Res., 91*(D), 7889–7895, 1986.

Logan, J., Nitrogen oxides in the troposphere: Global and regional budgets, *J. Geophys. Res., 88*(C), 10,785–10,807, 1983.

Louis, J.-F., A parametric model of vertical eddy fluxes in the atmosphere, *Boundary Layer Meteorol., 17*, 187–202, 1979.

Maier-Reimer, E., Geochemical cycles in an ocean general circulation model: Preindustrial tracer distributions, *Global Biogeochem. Cycles, 7*, 645–677, 1993.

Maier-Reimer, E., U. Mikolajewicz, and K. Hasselmann, Mean circulation of the Hamburg LSG OGCM and its sensitivity to the thermohaline surface forcing, *J. Phys. Oceanogr., 23*, 731–757, 1993.

Manning, M.R., D.C. Lowe, W.H. Melhuish, R.J. Sparks, G. Wallace, and C.A.M. Brenninkmeijer, The use of radiocarbon measurements in atmospheric studies, *Radiocarbon, 32*, 37–58, 1990.

Marland, G., R.M. Rotty, and N.L. Treat, $CO_2$ from fossil fuel burning: Global distribution of emissions, *Tellus Ser. B, 37*, 243–258, 1985.

Matthews, E., and I. Fung, Methane emissions from natural wetlands: Global distribution, area, and environment of characteristics of sources, *Global Biogeochem. Cycles, 1*, 61–86, 1987.

McCulloch, A., P.M. Midgley, and D.A. Fisher, Distribution of emissions of chlorofluorocarbons (CFCs) 11, 12, 113, 114 and 115 among reporting and non-reporting countries in 1986, *Atmos. Environ., 28*, 2567–2582, 1994.

Michelsen, H.A., R.J. Salawitch, P.O. Weinberg, and J.G. Anderson, Production of $O(^1D)$ from photolysis of $O_3$, *Geophys. Res. Lett., 21*, 2227–2230, 1994.

Midgley, P.M., The production and release to the atmosphere of 1,1,1-trichloroethane (methyl chloroform), *Atmos. Environ., 23*, 2663–2665, 1989.

Midgley, P.M., and A. McCulloch, The production and global distribution of emissions to the atmosphere of 1,1,1-trichloroethane (methyl chloroform), *Atmos. Environ., 29*, 1601–1608, 1995.

Nakazawa, T., T. Machida, M. Tanaka, Y. Fujii, S. Aoki, and O. Watanabe, Differences of the atmospheric $CH_4$ concentration between the arctic and antarctic regions in preindustrial/preagricultural era, *Geophys. Res. Lett., 20*, 943–946, 1993.

Newell, R.W., J.W. Kidson, D.G. Vincent, and G.J. Boer, The general circulation of the tropical atmosphere and interactions with extratropical latitudes, vol. 2, MIT Press, Cambridge, Mass., 1974.

Prather, M., R. Derwent, D. Ehhalt, P. Fraser, E. Sanhueza, and X. Zhou, Other trace gases and atmospheric chemistry, in *Climate Change 1994—Radiative Forcing of Climate Change and an Evaluation of the IPCC IS92 Emission Scenarios*, edited by J. T. Houghton, L. G. Meira Filho, J. Bruce, H. Lee, B. A. Callander, E. Haites, N. Harris, and K. Maskell, pp. 73–126, Cambridge Univ. Press, New York, 1995.

Price, C., and D. Rind, A simple lightning parametrization for calculating global lightning distributions, *J. Geophys. Res.*, *97*(D), 9919–9933, 1992.

Price, C. and D. Rind, Modeling global lightning distributions in a general circulation model, *Mon. Weather Rev.*, *122*, 1930–1937, 1994.

Prinn, R., et al., Global average concentration and trend for hydroxyl radicals deduced from ALE/GAGE trichloroethane (methyl chloroform) data for 1978–1990, *J. Geophys. Res.*, *97*(D), 2445–2462, 1992.

Prinn, R.G., R.F. Weiss, B.R. Miller, J. Huang, F.N. Alyea, D.M. Cunnold, P.B. Fraser, D.E. Hartley, and P.G. Simmonds, Atmospheric trends and lifetime of trichloroethane and global average hydroxyl radical concentrations based on 1978–1994 ALE/GAGE measurements, *Science*, *269*, 187–192, 1995.

Pszenny, A.A.P., W.C. Keene, D.J. Jacob, S. Fan, J.R. Maben, M.P. Zetwo, M. Springer-Young, and J.N. Galloway, Evidence of inorganic chlorine gases other than hydrogen chloride in marine surface air, *Geophys. Res. Lett.*, *20*, 699–702, 1993.

Quay, P.D., et al., Carbon isotopic composition of atmospheric $CH_4$: Fossil and biomass burning source strengths, *Global Biogeochem. Cycles*, *5*, 25–47, 1991.

Russell, G.L., and J.A. Lerner, A new finite-differencing scheme for the tracer transport equation, *J. Appl. Meteorol.*, *20*, 1483–1498, 1981.

Saueressig, G., P. Bergamaschi, J.N. Crowley, H. Fischer, and G.W. Harris, Carbon kinetic isotope effect in the reaction of $CH_4$ with Cl atoms, *Geophys. Res. Lett.*, *22*, 1225–1228, 1995.

Selzer, H., and W. Zittel, Klimawirksame Emissionen von Methangas—Untersuchung der weltweiten Methanemissionen aus der Nutzung fossiler Energieträger, der Abfallwirtschaft, der Landwirtschaft und der Erde, Rep. 10/90, *Ludwig-Bölkow-Systemtechnik GmbH*, Ottobrunn, Germany, 1990.

Singh, H.B., et al., Low ozone in the marine boundary layer of the tropical Pacific Ocean: Photochemical loss, chlorine atoms, and entrainment, *J. Geophys. Res.*, *101*(D), 1907–1917, 1996.

Spivakovsky, C.M., R. Yevich, J.A. Logan, S.C. Wofsy, M.B. McElroy, and M.J. Prather: 1990, Tropospheric OH in a Three-Dimensional Chemical Tracer Model: An Assessment Based on Observations of $CH_3CCl_3$, *J. Geophys. Res.*, *95*(D), 18,441–18,471, 1990.

Steele, L.P., P.J. Fraser, R.A. Rasmussen, M.A.K. Khalil, T.J. Conway, A.J. Crawford, R.H. Gammon, K.A. Masarie, and K.W. Thoning, The global distribution of methane in the troposphere, *J. Atmos. Chem.*, *5*, 125–171, 1987.

Steele, L.P., E.J. Dlugokencky, P.M. Lang, P.P. Tans, R.C. Martin, and K.A. Masarie, Slowing down of the global accumulation of atmospheric methane during the 1980s, *Nature*, *358*, 313–316, 1992.

Tans, P., A Note on Isotopic Ratios and the Global Atmospheric Methane Budget, *Global Biogeochem. Cycles*, in press, 1997.

Tarantola, A., Inverse Problem Theory, Elsevier, New York, 1987.

Tarantola, A., and B. Valette, Inverse problems = quest of information, *J. Geophys.*, *50*, 159–170, 1982a.

Tarantola, A., and B. Valette, Generalized nonlinear inverse problems solved using the least squares criterion, *Rev. Geophys.*, *20*, 219–232, 1982b.

Tiedtke, M., A comprehensive mass flux scheme for cumulus parametrization in large-scale models, *Mon. Weather Rev.*, *117*, 1779–1800, 1989.

Valentin, K.M., Numerical modeling of the climatological and anthropogenic influences on the chemical composition of the troposphere since the last glacial maximum, Ph.D. thesis, Fachbereich Geowissenschaften der Univ. Mainz, Mainz, Germany, 1990.

Wahlen, M., N. Tanaka, R. Henry, B. Deck, J. Zeglen, J. Vogel, J. Southon, A. Shemesh, R. Fairbanks, and W. Broecker, Carbon-14 in methane sources and in atmospheric methane: The contribution from fossil fuel carbon, *Science*, *245*, 286–290, 1989.

Wesely, M.L., Parametrization of surface resistances to gaseous dry deposition in regional-scale numerical models, *Atmos. Environ.*, *23*, 1293–1304, 1989.

Wingenter, O.W., M.K. Kubo, N.J. Blake, T.Y. Smith Jr., D.R. Blake, and S. Rowland, Hydrocarbon and halocarbon measurements as photochemical and dynamical indicators of atmospheric hydroxyl, atomic chlorine, and vertical mixing obtained during Lagrangian flights, *J. Geophys. Res.*, *101*(D), 4331–4340, 1996.

---

R. Hein and P. J. Crutzen, Max-Planck-Institut für Chemie, Abteilung Chemie der Atmosphäre, Postfach 3060, D-55020 Mainz, Germany. (email: hein@dkrz.de; air@mpch-mainz.mpg.de)

M. Heimann, Max-Planck-Institut für Meteorologie, Bundesstr. 55, D-20146 Hamburg, Germany. (email: heimann@dkrz.de)

(Received February 29, 1996; revised September 9, 1996; accepted September 18, 1996.)